united nations
educational, scientific
and cultural
organization

international atomic
energy agency

abdus salam
international centre for theoretical physics

H4.SMR/1241-17

"Workshop on Three-Dimensional Modelling
of Seismic Waves Generation and their Propagation"

25 September - 6 October 2000

TIME DEPENDENT GRAVITY FIELD PHYSICAL MODELLING OF DEEP AND SURFACE PROCESSES IN THE MEDITERRANEAN REGION

R. SABADINI

University of Milano
Milano, Italy

TIME DEPENDENT GRAVITY FIELD

PHYSICAL MODELLING OF DEEP AND SURFACE PROCESSES IN THE MEDITERRANEAN REGION

R. SABADINI
UNIV. OF MILAN

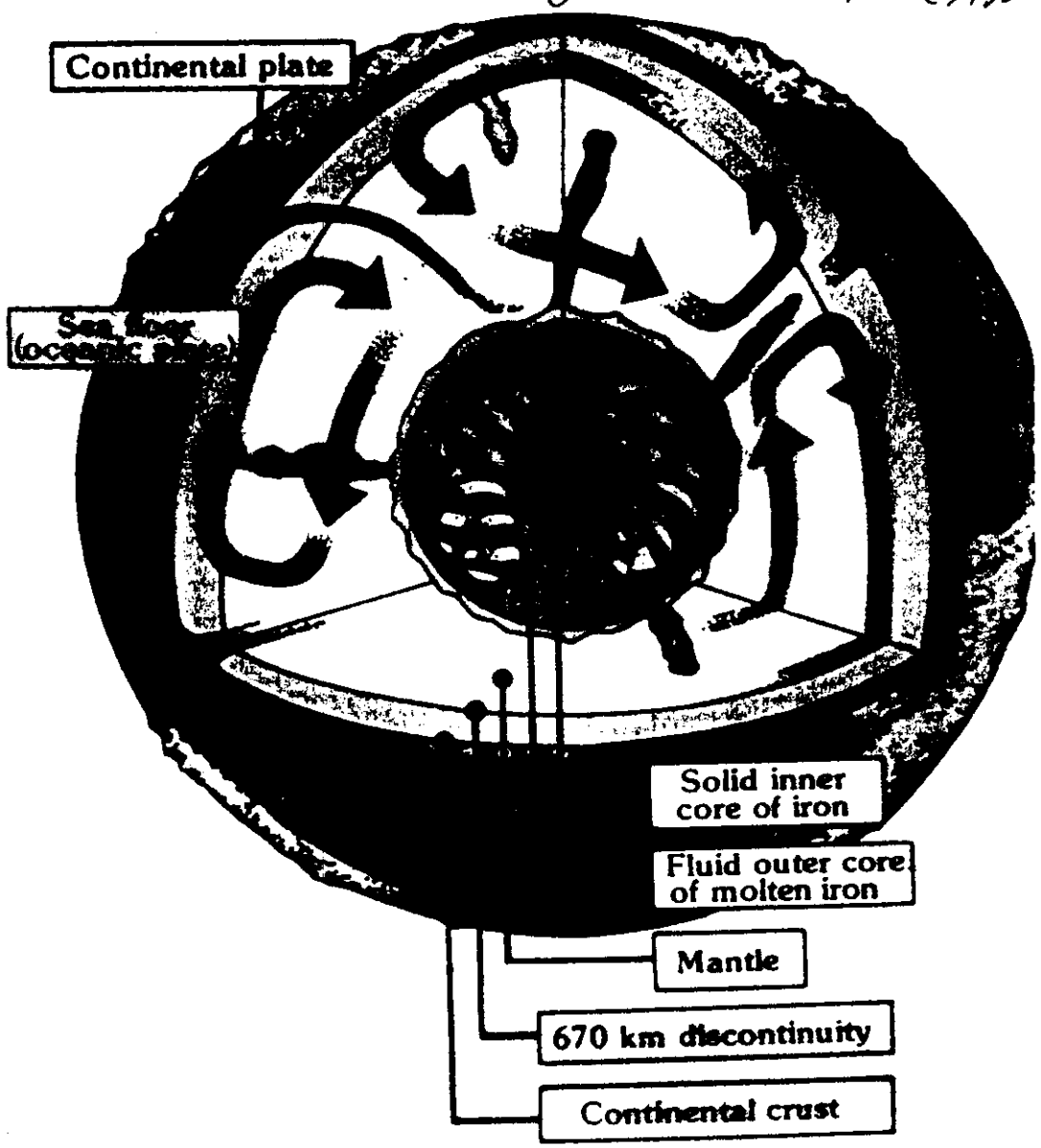

NEW PERSPECTIVES OPENED BY GEOPHYSICAL MODELLING AND BY CONSTRAINTS FROM THE GRAVITY AND DEFORMATION FIELDS

In the following decades, the major advancements in our understanding of the dynamics and time evolution of the Earth as an integrated system, including a variety of geophysical processes that affect the life of the human beings, will come from joint efforts in geophysics and geodesy, from a tight link between the mathematical modelling of the geophysical phenomena and the constraints provided by the gravity field, of its time dependent and static components, long and short wavelengths, and by geodetically detected crustal deformation rates.

GEOPHYSICAL MODELLING

Mantle dynamics
(Post-glacial rebound, sea-level changes)

Seismo-tectonics
(Active deformation, seismic hazard, sea-level changes)

Seismogenesis
(Earthquakes)

GRAVITY FIELD AND CRUSTAL DEFORMATION RATE

SLR (Satellite Laser Ranging, low harmonics, l=2, ...10)

GRACE (Satellite to Satellite Tracking, l=2,....50, time dependent)

GOCE (Gradiometry, l=40,.....250, static)

GPS (continuous GPS, 1-2 mm/yr)

SAR (2 cm)

PREDICTING THE TIME EVOLUTION OF THE EARTH

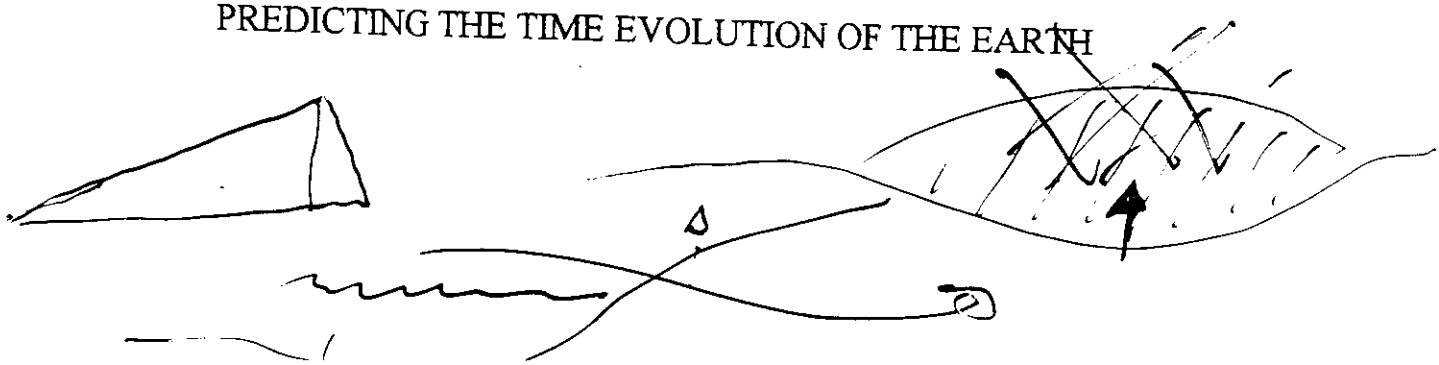

LONG TERM INSTABILITIES IN THE EARTH'S ROTATION, SEA LEVEL CHANGES AND OTHER GEODYNAMICAL PROCESSES

Applications of Normal Mode Relaxation Theory to Solid-Earth Geodynamics

(IN PRINT, BY KLUWER)

ROBERTO SABADINI
Dipartimento di Scienze della Terra, Sezione Geofisica, Università di Milano,
Via L. Cicognara 7, I-20129 Milano, Italy

BERT VERMEERSEN
Delft Institute for Earth-Oriented Space Research,
Faculty of Aerospace Engineering, Delft University of Technology,
Kluiverweg 1, NL-2629 HS Delft, The Netherlands

Kluwer Academic Publishers
Boston/Dordrecht/London

(WARNING! STILL TYPOS,...)

Contents

with $\vec{g}_0$ denoting the component in the initial state and $\vec{g}_1$ in the perturbed state.

The stress tensor σ can also be split into an initial part and incremental part, with, taking advection of initial (hydrostatic) pre-stress into account, reads:

$$\sigma_{ij} = \sigma_{ij,0} + \vec{u} \cdot \sigma_0 \delta_{ij} + \sigma_{ij,1} \tag{3.6}$$

with the initial hydrostatic stress condition $\sigma_{ij,0}$ given by:

$$\sigma_{ij,0} = -p_0 \delta_{ij} \tag{3.7}$$

and $\sigma_{ij,1}$ a tensor which describes the acquired, generally non-hydrostatic, stress. Combining (3.2) - (3.7) with (3.1) gives the following linearized balance of forces in the *deformed* situation:

$$-\nabla p_0 + \nabla \cdot \sigma_1 - \nabla(\rho_0 g \vec{u} \cdot \hat{e}_r) + \rho \vec{F} = 0 \tag{3.8}$$

The force $\vec{F}$ can generally be split into gravity and all kind of other forcings and loads (e.g. tidal forces, centrifugal forces, loads due to ice-water redistribution, earthquake forcings, etc.). Let us, for the moment, assume that the force $\vec{F}$ is the gravity (so essentially the condition of a free, self-gravitating Earth with no other forcings or loads acting on its surface or interior) and that, as it is a conservative force, it can be expressed as the negative gradient of the potential field ϕ:

$$\vec{F} = -\nabla \phi \tag{3.9}$$

The potential field ϕ can be written as

$$\phi = \phi_0 + \phi_1 \tag{3.10}$$

with ϕ_0 the field in the initial state and ϕ_1 the infinitesimal perturbation.

Combining (3.4) with (3.9) - (3.10) and inserting this in (3.8) leads to the following linearized equation of momentum:

$$\nabla \cdot \sigma_1 - \nabla(\rho_0 g_1 \vec{u} \cdot \hat{e}_r) - \rho_0 \nabla \phi_1 - \rho_1 g_0 \hat{e}_r = 0 \tag{3.11}$$

whereby use is made of the fact that, according to (3.1), in the initial state

$$\nabla \cdot \sigma_0 + \rho_0 \vec{F}_0 = \vec{0} \tag{3.12}$$

with $\vec{F}_0 = \vec{g}_0$ the volume force in the initial state. Note that there is not a term with ρ_1 in the advective term of (3.8), as this would combine with $\vec{u}$ to a second-order term. For the same reason the term $\rho_1 \phi_1$ does not occur in (3.11). Note also that the first term of (3.8) is canceled by the term $-\rho_0 \nabla \phi_0$, as

$$\nabla p_0 = \rho_0 \nabla \phi_0 \tag{3.13}$$

according to (3.2) and (3.9).

The first term of (3.12) describes the contribution from the stress, the second term the advection of the (hydrostatic) pre-stress, the third term the changed gravity (*self-gravitation*) and the fourth term the changed density (compressibility). In cases where self-gravitation is neglected, the third term will be zero, while in the case of incompressibility the fourth term will be zero.

The perturbed gravitational potential ϕ_1 satisfies the *Poisson equation*

$$\nabla^2\phi_1 = -4\pi G\rho_1 \tag{3.14}$$

with G the universal gravitational constant. In the case of incompressibility the right-hand term will be zero and (3.14) reduces to the *Laplace equation*

$$\nabla^2\phi_1 = 0 \tag{3.15}$$

Equations (3.11) and (3.14) (or (3.15) for incompressible deformation) need to supplemented with a constitutional equation describing how stress and strain (or strain rate) are related to each other, and for this we can, for instance, use the Maxwell model.

For the 3-D Maxwell model, stress and strain rate are related by

$$\dot{\sigma}_{ij} + \frac{\mu}{\eta}(\sigma_{ij} - \frac{1}{3}\sum_{k=1}^{3}\sigma_{kk}\delta_{ij}) = 2\mu\dot{\epsilon}_{ij} + \lambda\sum_{k=1}^{3}\dot{\epsilon}_{kk}\delta_{ij} \tag{3.16}$$

0.1 FUNDAMENTAL SOLUTIONS IN THE LAPLACE DOMAIN

In principle, deformation, stress field and gravity field for free Earth models can be solved by means of numerical integration techniques from the three equations (2.8), (2.10) or (2.11), and (2.12) with appropriate initial, boundary and continuity conditions. However, we will see that it is also possible to solve these equations virtually completely analytically by means of *normal model modeling* in the *Laplace transformed domain*. This analytical way of solving has a few great advantages: it leads us to a deeper insight in the mechanisms of the relaxation process with additional checking possibilities, and certainly for spherical (global) models they often prove easier to use than numerical integration techniques. Numerical integration techniques have also their advantages. For instance, they can generally easier deal with more elaborate models (e.g., those that use non-linear rheologies or lateral variations) and often prove simpler to use in half-space (regional) models. So the numerical and analytical models are more to be appreciated as being complimentary than redundant.

The Laplace transform $\tilde{F}(s)$ of a function $f(t)$ is defined by

$$\tilde{F}(s) = \int_{-\infty}^{\infty} f(t)e^{-st}dt \tag{3.17}$$

$$\frac{d^2}{d\theta^2}P_l(\theta) + \cot\theta\frac{d}{d\theta}P_l(\theta) = -l(l+1)P_l(\theta) \tag{3.51}$$

It is also necessary to make use of the derivative of the Legendre equation

$$\frac{d}{d\theta}[\frac{d^2}{d\theta^2}P_l(\theta) + \cot\theta\frac{d}{d\theta}P_l(\theta) + l(l+1)P_l(\theta)] = 0 \tag{3.52}$$

$$\frac{d^3}{d\theta^3}P_l + \frac{d^2}{d\theta^2}P_l\cot\theta - \frac{d}{d\theta}P_l[1 + \cot^2\theta + l(l+1)] = 0 \tag{3.53}$$

$$-(\frac{\mu}{r^2})[2l(l+1)v + v] \tag{3.54}$$

From the expression of the divergence $\nabla\cdot$ in spherical coordinates it is possible to express Δ in terms of the harmonic components of the displacement vector. From $\Delta = \nabla\cdot\mathbf{u}$

$$\chi_l = \dot{U}_l + 2r^{-1}U_l - l(l+1)V_l r^{-1} \tag{3.55}$$

The solution vector is defined by

$$\begin{aligned}
y_1 &= U_l \\
y_2 &= \tfrac{r\dot{U}_l + 2U_l}{l(l+1)} \\
y_3 &= T^l_{r_r} = \Pi_l + 2\mu\dot{U}_l \\
y_4 &= T^l_{r_\theta} = \mu(\dot{V}_l - \tfrac{V_l}{r} + \tfrac{U_l}{r}) \\
y_5 &= -\phi_l \\
y_6 &= -\dot{\phi}_l - \tfrac{l(l+1)}{r}\phi_l + 4\pi G\rho_0 U_l
\end{aligned} \tag{3.56}$$

where $\Pi_l = \lambda\chi_l$. The quantity y_6 is for obvious reasons sometimes nicknamed the *potential stress*. Why this parameter Q is chosen rather than $d\phi/dr$ will become clear when the boundary conditions are discussed in the next section.

Exercise. Prove that with the above definition of solution vector, the momentum and Laplace equations can be cast in the matrix form

$$\frac{d}{dr}\mathbf{y} = \mathbf{A}\cdot\mathbf{y} \tag{3.57}$$

where

$$\mathbf{A}_l(r,s) = \begin{pmatrix} -\frac{2\lambda}{\beta r} & \frac{l(l+1)\lambda}{\beta r} & \frac{1}{\beta} & 0 & 0 & 0 \\ -\frac{1}{r} & \frac{1}{r} & 0 & \frac{1}{\mu} & 0 & 0 \\ \frac{4}{r}\left(\frac{\gamma}{r}-\rho g\right) & -\frac{l(l+1)}{r}\left(\frac{2\gamma}{r}-\rho g\right) & -\frac{4\mu}{\beta r} & \frac{l(l+1)}{r} & \frac{\rho(l+1)}{r} & -\rho \\ -\frac{1}{r}\left(\frac{2\gamma}{r}-\rho g\right) & -\frac{2\mu-l(l+1)(\gamma+\mu)}{r^2} & -\frac{\lambda}{\beta r} & -\frac{3}{r} & -\frac{\varrho}{r} & 0 \\ -4\pi G\rho & 0 & 0 & 0 & -\frac{l+1}{r} & 1 \\ -\frac{4\pi G\rho(l+1)}{r} & \frac{4\pi G\rho l(l+1)}{r} & 0 & 0 & 0 & \frac{l-1}{r} \end{pmatrix} \tag{3.58}$$

with

$$\beta(s) = \lambda(s) + 2\mu(s) \tag{3.59}$$

and

$$\gamma(s) = \mu(s)\frac{3\lambda(s)+2\mu(s)}{\lambda(s)+2\mu(s)} \tag{3.60}$$

In the incompressible case the Lamé parameter λ becomes infinitely large in such a way that $\lambda\nabla\cdot u(s)$ is finite and equal in magnitude to the isotropic pressure. For the incompressible case, (2.17) results in $\lambda(s)\to\infty$, implying that $\beta(s)\to\infty$ according to (2.37), and $\gamma(s)\to\mu(s)$ according to (2.38). With this, the matrix (2.36) becomes for the incompressible case

$$\mathbf{A}_l(r,s) = \begin{pmatrix} -\frac{2}{r} & \frac{l(l+1)}{r} & 0 & 0 & 0 & 0 \\ -\frac{1}{r} & \frac{1}{r} & 0 & \frac{1}{\mu} & 0 & 0 \\ \frac{4}{r}\left(\frac{3\mu}{r}-\rho g\right) & -\frac{l(l+1)}{r}\left(\frac{6\bar{\mu}}{r}-\rho g\right) & 0 & \frac{l(l+1)}{r} & \frac{\rho(l+1)}{r} & -\rho \\ -\frac{1}{r}\left(\frac{6\mu}{r}-\rho g\right) & \frac{2(2l^2+2l-1)\mu}{r^2} & -\frac{1}{r} & -\frac{3}{r} & -\frac{\varrho}{r} & 0 \\ -4\pi G\rho & 0 & 0 & 0 & -\frac{l+1}{r} & 1 \\ -\frac{4\pi G\rho(l+1)}{r} & \frac{4\pi G\rho l(l+1)}{r} & 0 & 0 & 0 & \frac{l-1}{r} \end{pmatrix} \tag{3.61}$$

3. ANALYTICAL SOLUTION FOR THE INCOMPRESSIBLE CASE

From the condition of incompressibility

$$\chi_l = 0 \tag{3.62}$$

and homogeneity of each layer

$$\dot{\rho}_0 = 0 \tag{3.63}$$

we obtain for the Laplace and momentum equations

$$\ddot{\phi} + \frac{2}{r}\dot{\phi} - \frac{l(l+1)}{r^2}\phi = 0 \tag{3.64}$$

$$\begin{aligned} 0 &= \rho_0\dot{\phi}_l - \rho_0\partial_r(g_0U) + \partial_r(\Pi + 2\mu\dot{U}) \\ &+\tfrac{\mu}{r^2}\{4\dot{U}_r - 4U + l(l+1)(-U - r\dot{V} + 3V)\} \end{aligned} \tag{3.65}$$

$$\begin{aligned} 0 &= \rho_0\phi - \rho_0 g_0 U + \Pi + \mu r\partial_r(\dot{V} - \tfrac{V}{r} + \tfrac{U}{r}) \\ &+\tfrac{\mu}{r}\{5V + 3r\dot{V} - V - 2l(l+1)V\} \end{aligned} \tag{3.66}$$

By definition

$$\nabla_r^2 = \partial_r^2 + \frac{2}{r}\partial_r - \frac{l(l+1)}{r^2} \tag{3.67}$$

From () deriving ()with respect to r, summing and subtracting () we obtain

$$\nabla_r^2(\rho_0\phi - \rho_0 g_0 U + \Pi) = 0 \tag{3.68}$$

From (), collecting the derivative with respect to r

$$\partial_r(\rho_0\phi - \rho_0 g_0 U + \Pi) = -2\mu\ddot{U} - \frac{\mu}{r^2}\{4\dot{U}r - 4U + l(l+1)(-U - r\dot{V} + 3V)\} \tag{3.69}$$

The right hand side can be put in the form

$$2\mu\ddot{U} - \frac{\mu}{r^2}[4\dot{U}r - 4U - l(l+1)U - rl(l+1)\dot{V} + 3l(l+1)V] \tag{3.70}$$

that becomes with () and ()

$$-\mu\ddot{U} - 4\frac{\mu}{r}\dot{U} - 2\frac{\mu}{r^2}U + \frac{\mu}{r^2}l(l+1)U \tag{3.71}$$

Multiplying by r^2 () becomes

$$\mu r^2\ddot{U} + 4\mu r\dot{U} + 2\mu U - \mu l(l+1)U = \rho_0 r^2\partial_r(g_0U - \Pi - \phi) \tag{3.72}$$

We define

$$\rho_0 g_0 U - \rho_0\phi - \Pi = \Gamma \tag{3.73}$$

Exercise. Show that the solution of the Laplace equation takes the form
It is possible to demonstrate that the solution of () takes the following form

$$\phi = c_3 r^l + c_3^* r^{-(l+1)} \tag{3.74}$$

where r^l denotes the regular solution in $r = 0$ and $r^{-(l+1)}$ denotes the singular one.

Γ takes the following form, with the same dependence of ϕ with respect to r

$$\Gamma = \mu c_1 r^l + \mu c_1^* r^{-(l+1)} \tag{3.75}$$

The homogeneous equation

$$r^2\ddot{U} + 4r\dot{U} + 2U - l(l+1)U = 0 \tag{3.76}$$

obtained from (52) has two solutions, a regular one

$$c_2 r^{-(l+1)} \tag{3.77}$$

and a singular one

$$c_2^* r^{-(l+2)} = \frac{c_2^*}{r^{(l+2)}} \tag{3.78}$$

A particular solution for the regular component can be obtained substituting the regular component of Γ, providing

$$r^2\ddot{U} + 4r\dot{U} + 2U - l(l+1)U = r^2 c_1 l r^{(l-1)} \tag{3.79}$$

The regular solution is thus

$$\frac{c_1 l}{2(2l+3)} r^{(l+1)} \tag{3.80}$$

The singular component of the solution becomes, with the same procedure

$$c_1^* \frac{(l+1)}{2(2l-1)} r^{-l} \tag{3.81}$$

Summing up all the contributions we obtain

$$U_l = \frac{c_1 l r^{(l+1)}}{2(2l+3)} + c_2 r^{(l-1)} + \frac{c_1^*(l+1)}{2(2l-1)} r^{-l} + c_2^* r^{-(l+2)} \tag{3.82}$$

From () and () we obtain

$$\begin{aligned} V = {} & c_1 \tfrac{l+3}{2(2l+3)(l+1)} r^{l+1} + \tfrac{c_2}{l} r^{l-1} \\ & + c_1^* \tfrac{2-l}{2l(2l-1)} r^{-l} - \tfrac{c_2^*}{l+1} r^{-(l+2)} \end{aligned} \tag{3.83}$$

Exercise. Verify that with the definitions of the solution vector, y_3, y_4 and y_6 take the form

$$\begin{aligned} y_3 &= c_1\left[\tfrac{2\mu l(l+1)r^l+\rho_0 A l r^{l+2}}{2(2l+3)}\right] + c_2[\rho_0 A r^l + 2\mu(l-1)r^{l-2}] \\ &+c_3[-\rho_0 r^l] + c_1^*\left[\tfrac{-2\mu l(l+1)r^{-(l+1)}+\rho_0 A(l+1)l^{-(l+1)}}{2(2l-1)}\right] \\ &+c_2^*[-2\mu(l+2)r^{-(l+3)} + \rho_0 A r^{-(l+1)}] + c_3^*[-\rho_0 r^{-(l+1)}] \end{aligned} \tag{3.84}$$

$$\begin{aligned} y_4 &= c_1\tfrac{l(l+2)}{(2l+3)(l+1)}r^l + c_2\tfrac{2(l-1)}{l}r^{(l-2)} \\ &+c_1^*\tfrac{2(l^2-1)}{2l(2l-1)}r^{-(l+1)} + c_2^*\tfrac{2(l+2)}{l+1}r^{-(l+3)} \end{aligned} \tag{3.85}$$

$$\begin{aligned} y_6 &= +c_1\tfrac{3Alr^{l+1}}{2(2l+3)} + 3Ac_2 r^{l-1} - c_3(2l+1)r^{l-1} \\ &+c_1^*\tfrac{3A(l+1)}{2(2l-1)}r^{-l} + 3Ac_2^* r^{-(l+2)} \end{aligned} \tag{3.86}$$

For each of the N layers of the Earth model (assuming that each layer has material parameters which are constant inside it, while also the gravity g is assumed to be constant inside such a layer), the solution can be written as

$$\mathbf{y}_l(r,s) = \mathbf{Y}_l(r,s)\cdot\mathbf{C}_l(r) \tag{3.87}$$

in which $\mathbf{Y}_l$ is the *fundamental matrix* and $\mathbf{C}_l$ a 6-vector integration constant.

The fundamental matrix $\mathbf{Y}_l(r,s)$ reads

$$\begin{pmatrix} \frac{lr^{l+1}}{2(2l+3)} & r^{l-1} & 0 & \frac{(l+1)r^{-l}}{2(2l-1)} & r^{-l-2} & 0 \\ \frac{(l+3)r^{l+1}}{2(2l+3)(l+1)} & \frac{r^{l-1}}{l} & 0 & \frac{(2-l)r^{-l}}{2l(2l-1)} & -\frac{r^{-l-2}}{l+1} & 0 \\ \frac{(l\rho gr+2(l^2-l-3)\mu)r^l}{2(2l+3)} & (\rho gr+(2l-1)\tilde{\mu})r^{l-2} & -\rho r^l & \frac{(l+1)\rho gr-2(l^2+3l-1)\mu}{2(2l-1)r^{l+1}} & \frac{\rho gr-2(l+2)\mu}{r^{l+3}} & -\frac{\rho}{r^{l+1}} \\ \frac{l(l+2)\mu r^l}{(2l+3)(l+1)} & \frac{2(l-1)\mu r^{l-2}}{l} & 0 & \frac{(l^2-1)\mu}{l(2l-1)r^{l+1}} & \frac{2(l+2)\mu}{(l+1)r^{l+3}} & 0 \\ 0 & 0 & -r^l & 0 & 0 & -\frac{1}{r^l} \\ \frac{2\pi G\rho l r^{l+1}}{2l+3} & 4\pi G\rho r^{l-1} & -(2l+1)r^{l-1} & \frac{2\pi G\rho(l+1)}{(2l-1)r^l} & \frac{4\pi G\rho}{r^{l+2}} & 0 \end{pmatrix} \tag{3.88}$$

Each column of this fundamental matrix represents an independent solution of (2.34) with $\tilde{\mathbf{A}}$ given by (2.39).

A is defined by

$$A = \frac{4}{3}\pi g\rho_0 \tag{3.89}$$

The inverse of the fundamental matrix $\mathbf{Y}$ has the form

$$\mathbf{Y}_l^{-1}(r,s) = \mathbf{D}_l(r)\tilde{\tilde{\mathbf{Y}}}_l(r,s) \tag{3.90}$$

with $\tilde{\mathbf{D}}$ being a diagonal matrix with elements

$$\mathrm{diag}(\mathbf{D}_l(r)) = \frac{1}{2l+1}\left(\frac{l+1}{r^{l+1}}, \frac{l(l+1)}{2(2l-1)r^{l-1}}, -\frac{1}{r^{l-1}}, lr^l, \frac{l(l+1)}{2(2l+3)}r^{l+2}, -r^{l+1}\right) \tag{3.91}$$

and

$$\tilde{\mathbf{Y}}_l(r,s) = \begin{pmatrix} \frac{\rho g r}{\mu} & -2(l+2) & 2l(l+2) & -\frac{r}{\mu} & \frac{lr}{\mu} & \frac{\rho r}{\mu} & 0 \\ -\frac{\rho g r}{\mu} + \frac{2(l^2+3l-1)}{l+1} & & -2(l^2-1) & \frac{r}{\mu} & \frac{(2-l)r}{\mu} & -\frac{\rho r}{\mu} & 0 \\ 4\pi G\rho & & 0 & 0 & 0 & 0 & -1 \\ \frac{\rho g r}{\mu} & +2(l-1) & 2(l^2-1) & -\frac{r}{\mu} & -\frac{(l+1)r}{\mu} & \frac{\rho r}{\mu} & 0 \\ -\frac{\rho g r}{\mu} - \frac{2(l^2-l-3)}{l} & & -2l(l+2) & \frac{r}{\mu} & \frac{(l+3)r}{\mu} & -\frac{\rho r}{\mu} & 0 \\ 4\pi G\rho r & & 0 & 0 & 0 & 2l+1 & -r \end{pmatrix} \tag{3.92}$$

Although it would be quite laborious to derive such an analytical compact form of a 6×6 inverse matrix 'by hand', this can easily be done nowadays by means of an algebraic software package like *Mathematica*. Of course, it is not so difficult to show analytically that $\tilde{\mathbf{Y}} \times \tilde{\mathbf{Y}}^{-1} = \mathbf{I}$, with $\mathbf{I}$ the identity matrix, by hand!

3.1 TOROIDAL SOLUTION FOR THE INCOMPRESSIBLE CASE

The analogous of the A matrix for the toroidal case has been obtained by Alterman, Jarosh and Pekeris (1959) for the elqastic case, that remains valid also for the viscoelastic case once the Correspondence Principle is considered. It reads, with the superscript T to distinguish the toroidal case

$$\mathbf{A}_l^T(r,s) = \begin{pmatrix} \frac{1}{r} & \frac{1}{\mu(s)} \\ \frac{\mu(s)(l(l+1)-2)}{r^2} & \frac{-3}{r} \end{pmatrix} \tag{3.93}$$

The vector solution $\mathbf{y}^T$ is given by

$$y_1 = t_l^m y_2 = \mu(s)\left(\frac{dt_l^m}{dr} - \frac{t_l^m}{r}\right) \tag{3.94}$$

Exercise. Show that the l component of the fundamental solution is given by

$$\mathbf{Y}_l^T(r,s) = \begin{pmatrix} r^l & r^{-l-1} \\ \mu(s)(l-1)r^{l-1} & -\mu(s)(l+2)r^{-l-2} \end{pmatrix} \tag{3.95}$$

The inverse matrix of the fundamental solution reads

$$\mathbf{Y}^T(r,s) = \begin{pmatrix} \frac{2+l}{r^l(1+2l)} & \frac{r^{1-l}}{\mu(1+2l)} \\ \frac{r^{1+l}(l-1)}{1+2l} & \frac{r^{2+l}}{-\mu(1+2l)} \end{pmatrix} \tag{3.96}$$

3.2 SOLUTION FOR AN ARBITRARY FORCING SOURCE

After the solution for the homogeneous system of ordinary differential equations has been provided, it is now necessary to derive the solution of the non-homogeneous equations that account for the forcing term $\vec{F}$ entering equation (3.1), to deal with surface or internal loads, centrifugal forces and seismic dislocations.

The general solution of the non-homogeneous system of ordinary differential equations, where $\mathbf{f}$ is the vector characterizing the source

$$\frac{d}{dr}\mathbf{y} = \mathbf{A}\cdot\mathbf{y} + \mathbf{f} \tag{3.97}$$

is given by

$$\mathbf{y}(r) = \mathbf{Y}(r)[\int_{r_0}^{r} \mathbf{Y}^{-1}(r')\mathbf{f}(r')dr' + \mathbf{Y}^{-1}(r_0)\mathbf{y}(r_0)] \tag{3.98}$$

In the following derivation it is assumed that the source is embedded in the outermost layer of radius a, detoting the radius of the Earth, and internal radius b, denoting the interface between the bottom of the lithosphere and underlying layer. This procedure can generalized to a source embedded in an arbitrary internal layer. If the vector $\mathbf{f}$ has this form

$$\mathbf{f} = \mathbf{f}\delta(r - r_s) \tag{3.99}$$

with r_s denoting the radius of the source the non homogeneous system of ordinary differential equations takes the following form

$$\mathbf{y}(r) = \begin{cases} \mathbf{Y}(r)[\mathbf{Y}^{-1}(r_s)\mathbf{I}\mathbf{f} + \mathbf{Y}^{-1}(b)\mathbf{y}(b)], & r_s \le r \le a; \\ \mathbf{Y}(r)\mathbf{Y}^{-1}(b)\mathbf{y}(b), & b \le r \le r_s; \end{cases} \tag{3.100}$$

Exercise. Show that, if the forcing vector has the form

$$\mathbf{f} = \mathbf{f}\delta(r - r_s) + \mathbf{f}'\delta'(r - r_s) \tag{3.101}$$

the solution is given by

$$\mathbf{y}(r) = \begin{cases} \mathbf{Y}(r)[\mathbf{Y}^{-1}(r_s)(\mathbf{If} + \mathbf{A}(r_s)\mathbf{f}') + \mathbf{Y}^{-1}(b)\mathbf{y}(b)] & r_s \leq r \leq a; \\ \mathbf{Y}(r)\mathbf{Y}^{-1}(b)\mathbf{y}(b), & b \leq r \leq r_s; \end{cases} \tag{3.102}$$

4. PROPAGATOR MATRIX TECHNIQUE

For each layer of a spherical Earth model the solution vector (2.39) can be determined from the fundamental matrix. This solution vector expresses the most general solution for the displacements (radial and lateral), the stresses (radial and lateral), the gravity and the parameter y_6 from which the gravity gradient can be derived, for each layer of the spherical model and for each harmonic degree l in the Laplace domain. Each viscoelastic layer of the model is bounded by either another internal viscoelastic layer or an external layer (free outer surface, inviscid outer core layer at the core-mantle boundary). For each of these cases we need to determine the *boundary conditions*.

The *internal boundary conditions* are quite easy: for a boundary between two viscoelastic layers we require that U_l, V_l, σ_{rrl}, $\sigma_{r\theta l}$ and ϕ_l are continuous. This implies that during deformation there will be no 'cavitation' and no slip, while it is also assumed that no material crosses the boundary (otherwise we should have considered continuity of flow, ρU_l, rather than U_l). Internal boundaries where no material crosses are called *chemical boundaries*. Internal boundaries where material does cross, undergoing a phase change, are called *phase-change boundaries*. The boundary between the upper mantle and lower mantle at about 670 km depth is likely to be partly a chemical and partly a phase-change boundary, but we will assume here that in our Earth models there are only chemical boundaries.

As was already alluded to when the parameter y_6 was defined in (2.34), we do not take the gravity gradient as sixth component of the solution vector but a combination of gravity, gravity gradient and radial displacement. The reason becomes clear when the boundary condition for the gravity gradient at the free outer surface of the model is considered. If ϕ^e denotes the gravity of the external layer and ϕ of the top layer of the Earth model, then at the free surface

$$\frac{\partial \phi_l^e}{\partial r} - \frac{\partial \phi_l}{\partial r} = -4\pi G \rho U_l \tag{3.103}$$

As the gravity gradient of the external layer satisfies (note that ϕ proportional to $1/r^{n+1}$ is a solution of (2.10), while the other solution, being proportial to

r^n, becomes irregular at infinity)

$$\frac{\partial \phi_l^e}{\partial r} = -\frac{l+1}{r}\phi_l^e \tag{3.104}$$

and

$$\phi_l^e = \phi_l \tag{3.105}$$

we can express the external boundary condition as

$$y_6 = -\frac{\partial \phi}{\partial r} - \frac{l+1}{r}\phi + 4\pi G\rho U_l = 0 \tag{3.106}$$

With this it is clear that also y_6 is continuous for internal boundaries between viscoelastic layers.

At the interface $r = r_i$, the top layer i, in which

$$\mathbf{y}^{(i)}(r_i, s) = \mathbf{Y}^{(i)}(r_i, s)C^{(i)}(r_i) \tag{3.107}$$

can be linked to the layer $i+1$ below it, with

$$\vec{y}^{(i+1)}(r_i, s) = \mathbf{Y}^{(i+1)}(r_i, s)C^{(i+1)}(r_{i+1}) \tag{3.108}$$

by

$$y^{(i)} = y^{(i+1)} \tag{3.109}$$

as a consequence of the boundary conditions at the internal boundaries. With (2.50) it is possible to express the unknown constant vector $C^{(i)}$ into the unknown constant vector $C^{(i+1)}$. Doing this for every internal boundary of an N layer model (layer 1 is the top layer (crust or lithosphere), layers $2, 3, ..., N-1$ the layers below it, and layer N the core), the solution vector at the surface of the Earth at $r = a$ can be related to the conditions $C_l^{(N)}(r_c)$ at the core - mantle boundary (CMB) $r = r_c$ as

$$\mathbf{y}(a, s) = \left(\prod_{i=1}^{N-1} \mathbf{Y}_l^{(i)}(r_i, s)\mathbf{Y}^{(i)^{-1}}(r_{i+1}, s) \right) \mathbf{Y}^{(N)}(r_c, s)C^{(N)}(r_c) \tag{3.110}$$

The conditions at the CMB have been disputed among geophysicists since the 1960's. This controversy concentrates on the treatment of the continuity conditions for the vertical deformation at the CMB. Without going into details, if it is required that the vertical deformation at the CMB should be continuous, then this restricts the core to being either into a state of neutral equilibrium (homogeneous with neutral adiabatic temperature gradient) or that the radial stress at the CMB is zero. Both could be the case, but such restrictions are obviously not always the case in reality. Therefore the vertical deformation should in general not be continuous at the CMB. This might seem strange,

as one would think that this could lead to 'cavitation' or to overlap of layers occurring. The way out of this conundrum is that the fluid core layers are rather to be interpreted as *equipotentials* rather than *material layers*.

The gravity should be continuous at the CMB, at least: if we assume that there are no additional masses *positioned at* the CMB. Inside the core, the gravity should be proportional to r^l, as the other solution of (2.10) is irregular at the center of the Earth. Note that this is in contrast to the surface gravity that we used to derive (2.45). So for the lowermost mantle layer at the CMB we get

$$y_5^{(N)}(r_c) = K_1 r_c^l \tag{3.111}$$

with $y_5^{(N)}$ the fifth component of the vector $\mathbf{y}^{(N)}$ and K_1 a constant.

Assuming that the core is inviscid (fluid), we can readily deduce that the tangential displacement of the mantle is not restricted, so for the lowermost mantle layer at the CMB we can set

$$y_2^{(N)}(r_c) = K_2 \tag{3.112}$$

with K_2 a constant and $y_2^{(N)}$ the second component of the vector $\mathbf{y}^{(N)}$.

This leads to the following condition for the lowermost mantle layer at the CMB (note the minus sign of ϕ in (2.33)):

$$y_1^{(N)}(r_c) = \frac{y_5^{(N)}}{g_c} + K_3 = -\frac{3r_c^{l-1}}{4\pi G\rho_c} K_1 + K_3 \tag{3.113}$$

with g_c the gravity at the CMB, K_3 a constant, and $y_1^{(N)}$ the first component of the vector $y^{(N)}$.

The radial stress (pressure) should be continuous over the CMB. With (2.54) this leads for the lowermost mantle layer at the CMB to the condition

$$y_3^{(N)}(r_c) = g_c\rho_c K_3 = \frac{4}{3}\pi G\rho_c^2 r_c K_3 \tag{3.114}$$

with $y_3^{(N)}$ the third component of the vector $y^{(N)}$.

The tangential stress in the fluid core is zero, and thus continuity of stress requires for the lowermost mantle layer at the CMB that

$$y_4^{(N)}(r_c) = 0 \tag{3.115}$$

with $y_4^{(N)}$ the fourth component of the vector $y^{(N)}$.

Finally, the parameter Q should also be continuous at the CMB, leading for the lowermost mantle layer at the CMB to the condition ((2.52) and (2.54) in (2.34)):

$$y_6^{(N)}(r_c) = 2(l-1)r_c^{l-1}K_1 + 4\pi G\rho_c K_3 \tag{3.116}$$

with $y_6^{(N)}$ the sixth component of the vector $\mathbf{y}^{(N)}$.

If we treat the core as the innermost boundary layer, then with (2.52) - (2.57) the conditions at the CMB can be expressed as a 6×3 interface matrix $\mathbf{I}_{c,l}(r_c)$ as

$$\mathbf{Y}^{(N)}(r_c, s)\mathbf{C}^{(N)}(r_c) = \mathbf{I}_{c,l}(r_c) \cdot \mathbf{C_c} \tag{3.117}$$

with

$$\mathbf{I}_{c,l}(r_c) \;=\; \begin{pmatrix} -r_c^{l-1}/A_c & 0 & 1 \\ 0 & 1 & 0 \\ 0 & 0 & \rho_c A_c r_c \\ 0 & 0 & 0 \\ r_c^l & 0 & 0 \\ 2(l-1)r_c^{l-1} & 0 & 3A_c \end{pmatrix} \tag{3.118}$$

with ρ_c the (uniform) density of the core, $A_c = \frac{4}{3}\pi G\rho_c$, and $\vec{C}_c = (K_1, K_2, K_3)$ a 3-vector constant.

The solution vector $\mathbf{y}(a, s)$ (2.51) with (2.58) can either express the conditions for a free surface, or express the conditions for a (tidal) forcing or (surface) loading. The loading/forcing case will be treated in section 2.5.

The solution vector $\mathbf{y}(R, s)$ can be split into two parts: one part that contains the unconstrained parameters U_l, V_l and ϕ_l (which we are solving for), and the other containing the constrained $y_3 = \sigma_{rr}$, $y_4 = \sigma_{r\theta}$ and y_6.

For a free surface, the components of the latter, as we have seen already, are all zero at the surface. If P_1 denotes the *projection vector* of (2.51) with (2.58) on the third, fourth and sixth component of (2.51) with (2.58), then we get the following condition:

$$\mathbf{0} = \mathbf{P_1 y(a, s)} = \mathbf{P_1} \left(\prod_{\mathbf{i=1}}^{\mathbf{N-1}} \mathbf{Y^{(i)}(r_i, s)Y^{(i)^{-1}}(r_{i+1}, s)} \right) \mathbf{I_{c,l}(r_c)} \cdot \mathbf{C_c} \tag{3.119}$$

and this condition puts constraints on the s-values in the sense that only those s-values for which (with (2.58))

$$\det \left(P_1 \left(\prod_{i=1}^{N-1} \tilde{\mathbf{Y}}_l^{(i)}(r_i, s)\tilde{\mathbf{Y}}_l^{(i)^{-1}}(r_{i+1}, s) \right) \mathbf{I}_{c,l}(r_c) \right) \;=\; 0 \tag{3.120}$$

are non-zero solutions of (2.60). The expression (2.61) is called the *secular equation* and the determinant the *secular determinant*. Its solutions $s = s_j$ ($j = 1, 2, 3, ..., M$) are the inverse relaxation times of the M relaxation modes of the Earth model. These s_j are dependent on the harmonic degree l (and thus must be determined for each harmonic degree), but the index l is left away in order not to complicate the indexing. The total number of relaxation modes for each harmonic degree, M, is the same for each harmonic degree (with the exception

of degree 1, but we will not digress on the differences between degree 1 on the one hand and degrees 2 and higher any further).

Experience and (extremely laborious) analytical proofs have led to the following results:

- The surface contributes one mode, labeled $M0$.
- If there is an elastic lithosphere on top of a viscoelastic mantle, then there is one mode triggered by the lithosphere - mantle boundary, labeled $L0$.
- At the boundary of two viscoelastic layers, one *buoyancy mode* is triggered if the density on both sides of the boundary is different. Buoyancy modes between two mantle layers are usually labeled Mi, with $i = 1, 2, 3, ...$, whereby $M1$ is usually the buoyancy mode associated with the 670 km discontinuity (upper / lower mantle) and $M2$ with the 400 km discontinuity (shallow upper mantle / mantle transition zone).
- At the same boundary two additional *viscoelastic modes* are triggered if the Maxwell time on both sides of the boundary is different (so if the viscosity and rigidity are different, but the ratio of viscosity and rigidity not, then these viscoelastic modes are absent). These 'paired' modes are also called *transient modes* as they have relatively short relaxation times, and are therefore usually labeled Ti, with $i = 1, 2, 3, ...$
- The boundary between the lowermost mantle layer and the inviscid core contributes one mode, labeled $C0$.

It is thus possible, with the above rules, to determine the total amount of modes of (2.61). This is of importance, as solving (2.61) has to be done numerically. However, this root-solving is the only non-analytical part of the viscoelastic relaxation method as described in this chapter.

The root-solving procedure usually consists of two parts: *grid-spacing*, followed by a *bisection algorithm*. In the grid-spacing part, the s-domain is split into a number of discrete intervals. For each s-value at a boundary of an interval, the value of the determinant of (2.61) is calculated, after which this value is multiplied with the value of the determinant of the s-value of the boundary next to it. If this product is positive, then the determinant has not either not changed in sign (or has changed an even amount of times). If the product is negative, then we are sure that there is (at least) one root inside the interval bounded by the two s-values for which the determinant was calculated. In that case, the interval is split up in two parts, and the procedure of determining the product of the determinant of the bounding s-values is repeated. The interval where the determinant changes sign will result again in a negative product, and for this interval the procedure of cutting the interval in two, etc., is repeated. Thus the s-value where the determinant of (2.61) is equal to zero

Figure 3.3. Relaxation times in years as a function of the harmonic degree l and varying lower mantle viscosity. The parameter $C = \nu_{TZ}/\nu_{UM}$ is varied from 1 to 200. LB corresponds to $\nu_{UM} = \nu_{LM} = 10^{21}$ Pa s, while UB corresponds to $\nu_{UM} = 0.5\times10^{21}$ Pa s and $\nu_{LM} = 2\times10^{22}$ Pa s.

$$\mathbf{b} = \mathbf{P_1 y}_l(R,s) = P_1 \left(\prod_{i=1}^{N-1} \mathbf{Y}_l^{(i)}(r_i,s) \mathbf{Y}_l^{(i)^{-1}}(r_{i+1},s) \right) \mathbf{I}_{c,l}(r_c) \cdot \mathbf{C}_c \tag{3.123}$$

where $\mathbf{b}$ constrains $\tilde{\sigma}_{rrl}$, $\sigma_{r\theta l}$ and y_6 at the surface. For a Heaviside function mass load, the vector $\mathbf{b}$ reads

$$\mathbf{b} = (-\frac{1}{4\pi}g(R)(2l+1)/R^2\ ,\ 0\ ,\ -G(2l+1)/R^2)^T \tag{3.124}$$

The derivation of (2.89) will follow later.

The unconstrained parameters U_l, V_l and ϕ_l at the surface can be expressed as

$$\begin{aligned}(U_l, V_l, \ -\ \phi_l)^T(R,s) = P_2\mathbf{y}(R,s) = \\ = \left(P_2 \prod_{i=1}^{N-1} \mathbf{Y}_l^{(i)}(r_i,s)\mathbf{Y}_l^{(i)^{-1}}(r_{i+1},s)\mathbf{I}_{c,l}(r_c)\right)\cdot \mathbf{C}_c\end{aligned} \tag{3.125}$$

with P_2 the projection vector of (2.51) with (2.58) on the first, second and fifth component of (2.51) with (2.58).

Elimination of $\mathbf{C}_c$ from (2.88) and (2.90) results in

$$\begin{aligned}(U_l, V_l, \ -\ \phi_l)^T(R,s) = \left(\mathbf{P_2} \prod_{i=1}^{N-1} \mathbf{Y}^{(i)}(r_i,s)\mathbf{Y}^{(i)^{-1}}(r_{i+1},s)\mathbf{I}_{c,l}(r_c)\right)\cdot \\ \cdot\ \left(P_1 \prod_{i=1}^{N-1} \mathbf{Y}^{(i)}(r_i,s)\mathbf{Y}^{(i)^{-1}}(r_{i+1},s)\mathbf{I}_{c,l}(r_c)\right)^{-1}\cdot \mathbf{b}\end{aligned} \tag{3.126}$$

For each of the M solutions s_j of (2.61) we can now determine the solutions for U_l, V_l and ϕ_l by inverse-Laplace transformation using the *residue theorem* of the former section. The solution vector $\mathbf{P_2y}(r,s)$ can be written as the sum of an elastic term and M viscous terms:

$$\mathbf{P_2y}(r,s) = \mathbf{K}^e(r) + \sum_{j=1}^{M} \frac{\mathbf{K}^j(r)}{s-s_j} \tag{3.127}$$

in which the $\mathbf{K}^j(r)$ are the vector residues of the solution kernel vector $\mathbf{y}(r,s)$ given by

$$\left(\frac{\mathbf{P_2BI}_c(r_c)\cdot(\mathbf{P_1BI}_c(r_c))^\dagger}{\frac{d}{ds}\det(\mathbf{P_1BI}_c(r_c))}\right)_{s=s_j}\cdot \mathbf{b} \tag{3.128}$$

with

$$\mathbf{B} \ = \ \prod_{i=1}^{N-1} \mathbf{Y}^{(i)}(r_i,s)\mathbf{Y}^{(i)^{-1}}(r_{i+1},s) \tag{3.129}$$

and

$$(\mathbf{P_1BI}_c(r_c))^\dagger = (\mathbf{P_1BI}_c(r_c))^{-1} \cdot \det(\mathbf{P_1BI}_c(r_c)) \tag{3.130}$$

and $\mathbf{K}^e(r)$ the elastic limits

$$\mathbf{K}^e(r) = \lim_{s\to\infty} (\mathbf{P_2BI}_c(r_c) \cdot (\mathbf{P_1BI}_c(r_c))^{-1}) \cdot \mathbf{b} \tag{3.131}$$

This gives the radially dependent part of the *Green functions* for the variables for each degree l. Multiplying the Green functions with the Laplace transformed forcing functions (which is the same as a convolution in the space - time domain) and performing an inverse Laplace transformation gives the sought-for expressions.

The inverse Laplace transform $f(t)$ of a function $F(s)$ is formally defined by complex contour integration by (cf. (2.12))

$$f(t) = \frac{1}{2\pi i} \int_{\gamma-i\infty}^{\gamma+i\infty} F(s)e^{st}ds \tag{3.132}$$

in which the real constant γ is chosen such that singularities of $F(s)e^{st}$ are either *all* on the left or *all* on the right side of the vertical line running from $\gamma - i\infty$ to $\gamma + i\infty$. Closing the contour with a half-circle (either on the left of the line or on the right, depending on where the singularities are situated) leads to a complex contour that is known as the *Bromwich path.*

Applied to (2.92) gives for the Heaviside surface loading the solution

$$(U_l, V_l, -\phi_l)^T(r,t) = \mathbf{K}^e(r)\delta(t) + \sum_{j=1}^{M} \mathbf{K}^j(r)e^{s_j t} \tag{3.133}$$

Solution (2.96) shows that for each harmonic degree l, the horizontal displacement, vertical displacement and change in gravity consist of an immediate response to the (Heaviside) load (the elastic response), followed by M exponentially decaying (viscous) responses. At least, the viscous responses are decaying only if the inverse relaxation times s_j for each harmonic degree are *negative*. For incompressible models this turns out to be always the case if the Earth layers show no density inversions in the radial Earth profile. However, if there is a layer with a greater density than its neighboring layer below, then the buoyancy mode for the interface will have a positive inverse relaxation time for each harmonic degree l. Such a positive relaxation time leads, according to (2.96), to an exponentially increasing response in the displacements and gravity variations, and thus the interface becomes *Rayleigh-Taylor* unstable. If this occurs, convective motions will be triggered in the Earth model, and the linearization assumed in the normal-mode theory as developed in this chapter breaks down.

Figure 7. Retrieval times for all four MN and MO models with $\nu_1 = 2 \times 10^{-5}$ and 10^{-4} s^{-1} (e.g. a) and $\nu_1 = 10^{-4}$ and 10^{-3} s^{-1} (e.g. c) as a function of the number of patterns stored. Retrieval is to 90% of the initial overlap. Adjacent plots are for 1 and 8 bits per synapse. Data from Sompolinsky (1987) and Tsodyks & Feigel'man (1988).

7. DISLOCATION SOURCE

With respect to the surface loading, the boundary conditions for dislocations are the vanishing of the stress components and y_6 at the Earth's surface

$$y_3(a) = y_4(a) = y_6(a) = 0 \tag{3.134}$$

These conditions can be cast in the following form

$$\mathbf{P_2 Y(a)}[\mathbf{Y}^{-1}(r_s)(\mathbf{If} + \mathbf{A}(r_s)\mathbf{f}') + \mathbf{Y}^{-1}(b)\mathbf{y}(b)] = 0 \tag{3.135}$$

where $\mathbf{P_2}$ denotes the projection operator on the third, fourth and sixth component of the solution vector.

If the three component vector $\mathbf{b_F}$ is defined in the following way

$$\mathbf{b_F} = -\mathbf{P_2 Y(a)}\mathbf{Y}^{-1}(r_s)(\mathbf{If} + \mathbf{A}(r_s)\mathbf{f}') \tag{3.136}$$

the boundary conditions at the surface become

$$\mathbf{P_2 Y(a)}\mathbf{Y}^{-1}(b)\mathbf{y}(b)] = \mathbf{b_F} \tag{3.137}$$

With these definitions, the boundary conditions at the surface for dislocation sources become formally equivalent to those appropriate for surface loading.

8. MULTI-LAYER MODELS

8.1 INTRODUCTION

Multi-layer, spherically stratified, self-gravitating relaxation models with a large amount of layers (more than 100) can be dealt with analytically. Relaxation processes are studied for both Heaviside surface loads and tidal forcings. Simulations of the relaxation process of a realistic Earth model with an incompressible Maxwell rheology show that models containing about 30 to 40 layers have reached continuum limits on all timescales and for all harmonic degrees up to at least 150 whenever an elastic lithosphere is present, irrespective of the viscosity profile in the mantle. Especially fine-graded stratification of the shallow layers proofs to be important for high harmonic degrees in these models. The models produce correct long-time (fluid) limits. It is shown that differences in transient behaviour of the various models are due to the applied volume-averaging procedure of the rheological parameters. Our earlier proposed hypothesis that purported shortcomings in the fundamental physics of (discrete) normal mode theory are artificial consequences of numerical inaccuracies, theoretical mis-interpretations and using incomplete sets of normal modes is reinforced by the results presented. We show explicitly that the models produce both continuous behaviour resulting from continuous rheological stratifications and discrete behaviour resulting from sharp density contrasts, as at the outer surface and the core mantle boundary. The differences between

The linearized Liouville equation for polar wander (3.23) which includes both loading and tidal forcings can be written as

$$i\frac{\dot{\mathbf{m}}}{\sigma_\mathbf{r}} + \mathbf{m} = \mathbf{\Phi} \tag{4.49}$$

with the forcing function $\mathbf{\Phi}$ consisting of two parts: $\mathbf{\Phi} = \mathbf{\Phi_L} + \mathbf{\Phi_R}$, with $\mathbf{\Phi_L}$ the part describing the direct geodynamic forcing (e.g. an earthquake or changing atmospheric pressure) and $\mathbf{\Phi_R}$ the induced rotational deformation. With (3.47) the linearized Liouville equation (3.49) can be expressed as

$$i\frac{\dot{\mathbf{m}}}{\sigma_r} + (1 - \frac{k_2}{k_0})\mathbf{m} = \mathbf{\Phi_L} \tag{4.50}$$

or

$$i\frac{\dot{\mathbf{m}}}{\sigma_0} + \mathbf{m} = \mathbf{\Psi_L} \tag{4.51}$$

with

$$\sigma_0 = (1 - \frac{k_2}{k_0})\sigma_r \tag{4.52}$$

and

$$\mathbf{\Psi_L} = \frac{k_0}{k_0 - k_2}\mathbf{\Phi_L} \tag{4.53}$$

The term σ_0 in (3.51) is the frequency of the *Chandler wobble*. Its four months decrease with respect to the frequency of the *Eulerian free precession* frequency σ_r (3.15) is apparently due to the quotient k_2/k_0.

Exercise: Determine numerically k_0 and consequently k_2 from your answer to the exercise on page 31 and the observation that the frequency of the Chandler wobble is four months lower than the Eulerian precession frequency.

Exercise: Show, assuming that k_2 is not time-dependent, by solving the homogeneous form of (3.51) and consequently by the method of *variation of a constant*, that the solution of (3.51) is

$$\mathbf{m}(t) = -i\sigma_0 e^{i\sigma_0 t}\int_{-\infty}^{t} \mathbf{\Psi_L}(\tau)e^{-i\sigma_0\tau}d\tau \tag{4.54}$$

and determine $\mathbf{m}(t)$ for the following two cases:
(1) $\mathbf{\Psi_L}(t) = \mathbf{\Psi_0}H(t)$, with $\mathbf{\Psi_0}$ time-independent and H the Heaviside function;
(2) $\mathbf{\Psi_L}(t) = \mathbf{\Psi_0}\delta(t)$, with $\mathbf{\Psi_0}$ time-independent and δ the delta function.
Draw your solutions in the (m_1,m_2)-plane for both cases (1) and (2). Assume that at time $t = 0$ the rotation pole is at the origin.

Laplace transformation and substituting (4.23) leads to

$$\left(i\frac{s}{\sigma_r}+1-\frac{1}{k_f}\left(k_e+\sum_{i=1}^{M}\frac{k_i}{s-s_i}\right)\right)\tilde{\mathbf{m}}(s)=\tilde{\mathbf{\Phi}}_L(s) \tag{4.55}$$

with $k_f = k_2(s=0)$ being the tidal fluid Love number.

With the tidal elastic Love number

$$k_e = k_f + \sum_{i=1}^{M}\frac{k_i}{s_i} \tag{4.56}$$

(cf. (4.23)), and

$$\frac{k_i}{s_i}+\frac{k_i}{s-s_i}=\frac{k_i s}{s_i(s-s_i)} \tag{4.57}$$

(4.34) becomes

$$s\left(1+i\frac{\sigma_r}{k_f}\sum_{i=1}^{M}\frac{k_i}{s_i(s-s_i)}\right)\tilde{\mathbf{m}}(s)=-i\sigma_r\tilde{\mathbf{\Phi}}_L(s) \tag{4.58}$$

So

$$s\left(1+\sum_{i=1}^{M}\frac{x_i}{s-s_i}\right)\tilde{\mathbf{m}}(s)=-i\sigma_r\tilde{\mathbf{\Phi}}_L(s) \tag{4.59}$$

with

$$x_i = i\frac{\sigma_r k_i}{k_f s_i} \tag{4.60}$$

Now

$$1+\sum_{i=1}^{M}\frac{x_i}{s-s_i}=\frac{\prod_{j=1}^{M}(s-s_j)}{\prod_{j=1}^{M}(s-s_j)}+\sum_{i=1}^{M}x_i\frac{\prod_{j\neq i}^{M}(s-s_j)}{\prod_{j=1}^{M}(s-s_j)} \tag{4.61}$$

where $\prod_{j\neq i}^{M}$ means $\prod_{j=1}^{M}$ without the term $j=i$.

The right-hand side of (4.38)

$$\frac{\prod_{j=1}^{M}(s-s_j)+\sum_{i=1}^{M}x_i\prod_{j\neq i}^{M}(s-s_j)}{\prod_{j=1}^{M}(s-s_j)} \tag{4.62}$$

can be transformed into

$$\frac{\sum_{i=0}^{M}\alpha_i s^i}{\prod_{j=1}^{M}(s-s_j)} \tag{4.63}$$

(whereby it immediately follows that $\alpha_M = 1$), and consequently (4.38) can be put as

$$1+\prod_{i=1}^{M}\frac{x_i}{s-s_i}=\frac{\sum_{j=1}^{M}(s-a_j)}{\prod_{j=1}^{M}(s-s_j)} \tag{4.64}$$

with a_i being the M complex roots of the equation

$$\sum_{i=0}^{M} \alpha_i s^i = 0 \tag{4.65}$$

(4.39) in (4.36) gives

$$s \frac{\prod_{j=1}^{M}(s - a_j)}{\prod_{j=1}^{M}(s - s_j)} \tilde{\mathbf{m}}(s) = -i\sigma_r \tilde{\mathbf{\Phi}}_L(s) \tag{4.66}$$

and so

$$\begin{aligned} \tilde{\mathbf{m}}(s) &= -i\sigma_r \frac{\prod_{j=1}^{M}(s - s_j)}{s \prod_{j=1}^{M}(s - a_j)} \tilde{\mathbf{\Phi}}_L(s) \\ &= -i\sigma_r \left(\frac{\mathbf{A}_0}{s} + \sum_{j=1}^{M} \frac{A_j}{s - a_j} \right) \tilde{\mathbf{\Phi}}_L(s) \end{aligned} \tag{4.67}$$

In this expression, the terms $\mathbf{a}_j$ are the inverse relaxation times from the tidal problem for the M modes, having the strength given by the residues $\mathbf{A}_j$. The residue $\mathbf{A}_0$ gives the strength of the secular term.

Just as the sea-level equation (2.24) forms the basis for realistic models on sea-level variation that take solid-earth deformation self-consistently into account, equation (3.50) forms the basis of realistic models on Earth rotation that take solid-earth deformation and its consequential shifts of the equatorial bulge self-consistently into account (with one restriction: the Liouville expression has been linearized and therefore polar wander needs to be restricted to about 10 degrees over the Earth surface, or about 1000 km, at most). Of course, one can also combine (2.24) and (3.50) into an even more general theory. Interesting interactions between solid-earth deformation, sea-level variations and rotational changes then emerge (for instance, not only can sea-level variations induce polar wander, but polar wander could induce sea-level variations). One important ingredient has not been explicitly modeled, however, and that is the way the solid Earth deforms and changes its gravity field due to loads and forcings. To put it in technical terms: how *Love numbers* are to be determined once an Earth model is specified. As alluded to already in chapters 2 and 3, this rather complicated modeling by means of normal mode analysis will be dealt with in the 4th year course on *Geophysical Applications of Satellite Measurements*.

Whereas the present-day true polar wander and the secular non-tidal acceleration of the Earth have usually been attributed to post-glacial rebound, it was suggested in chapter 3 that non-glacially induced vertical tectonic movements taking place under non-isostatic conditions can also be effective in changing

Even Zonal Time Series

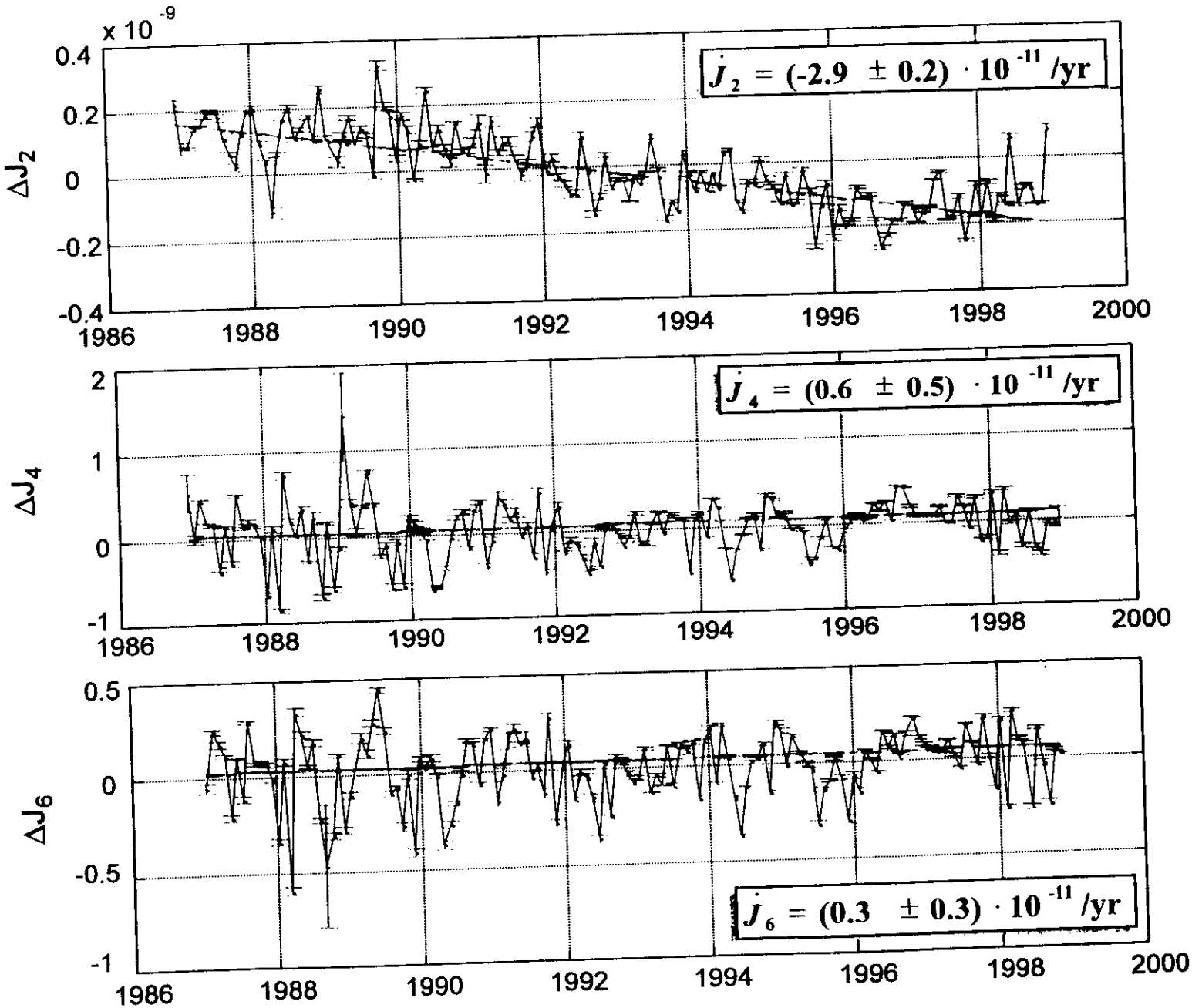

Odd Zonal Time Series

(obtained from Starlette observations only)

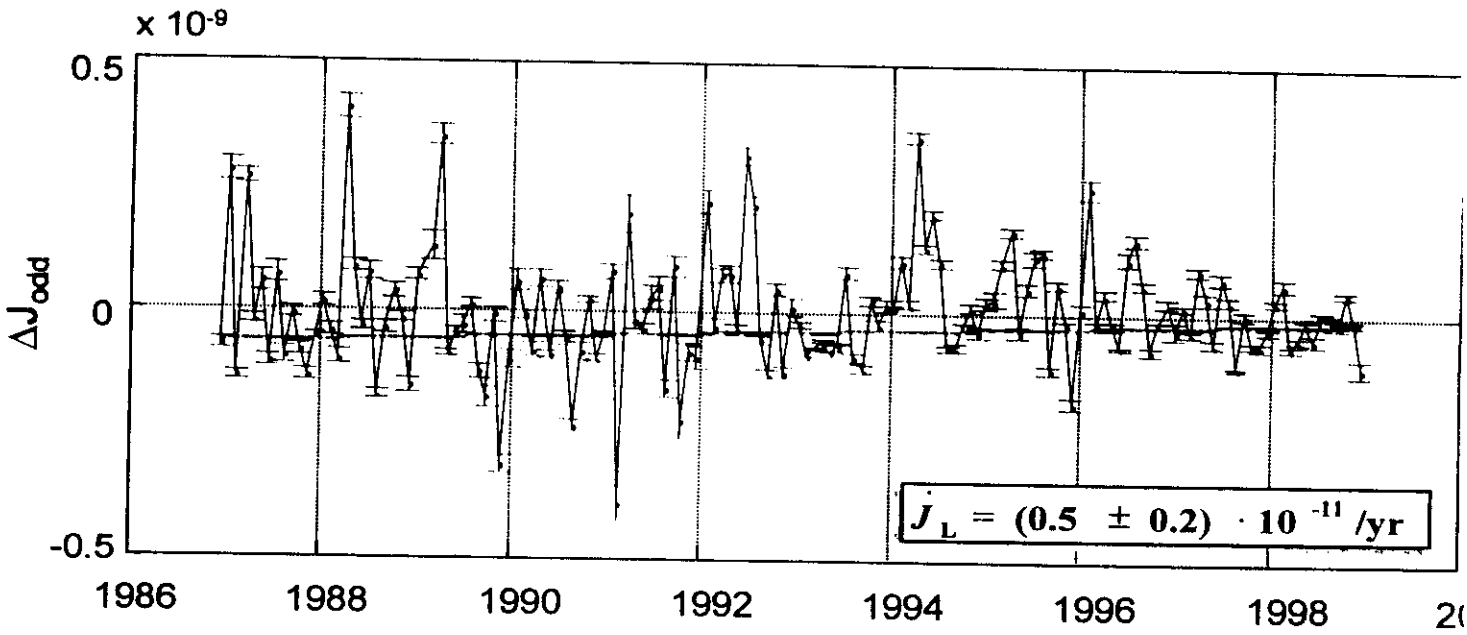

SLR

Long wavelength, time dependent

Harmonic degrees l=2,....6
with lumped odd zonals l=3,5

Solution from the Centre of Space Geodesy - Matera (Italian Space Agency)

PREDICTING

Global ongoing deformation of the Earth

Present-day mass instabilities in Anctarctica and Greenland

Secular component of sea-level variabilities due to post-glacial rebound and present-day glacial instabilities

Late Pleistocene deglaciation

Max. Antarctic + max. Greenland meltings

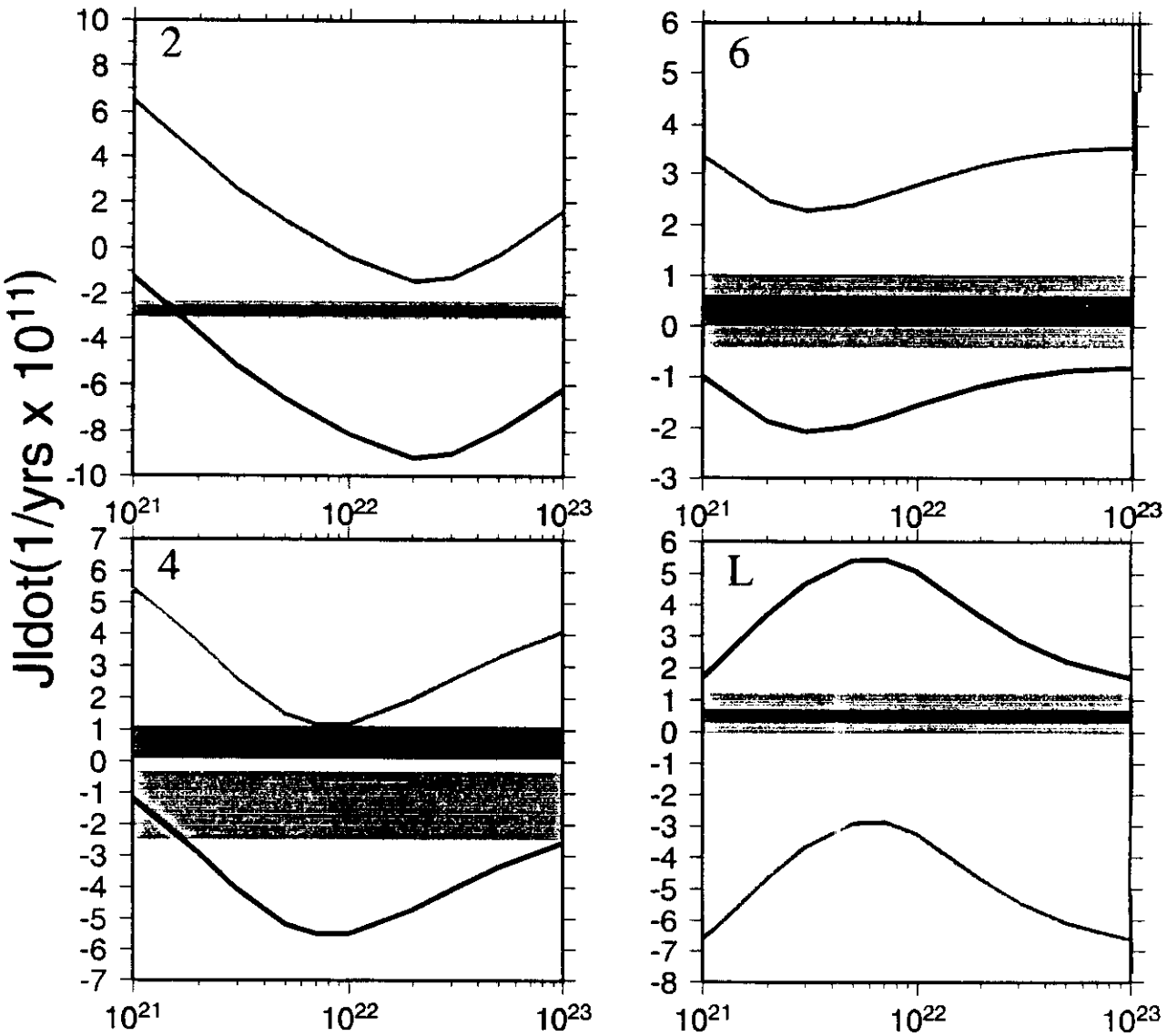

LOG CHISQUARE

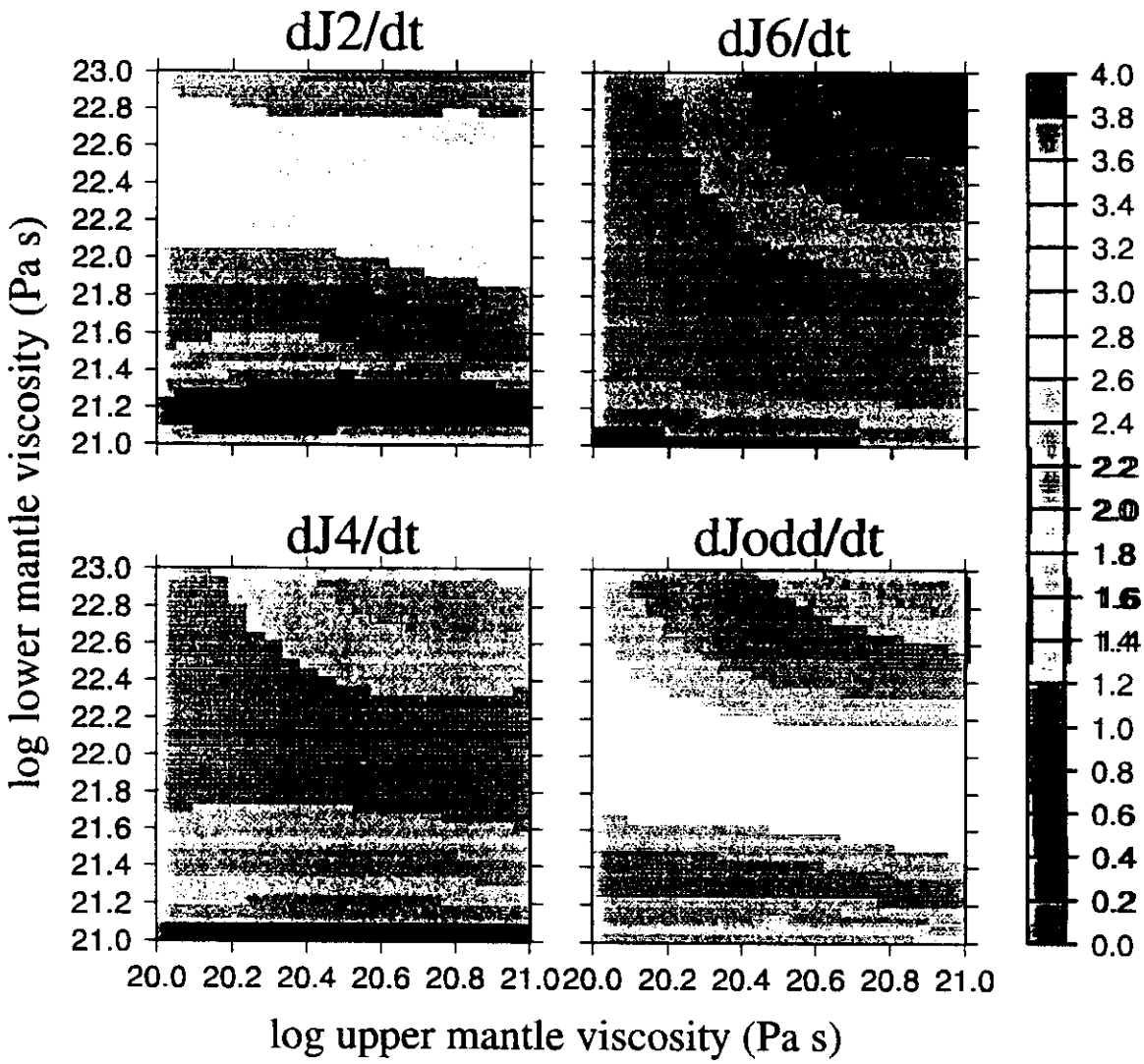

Data (Devoti et al. 2000)

LOG CHISQUARE

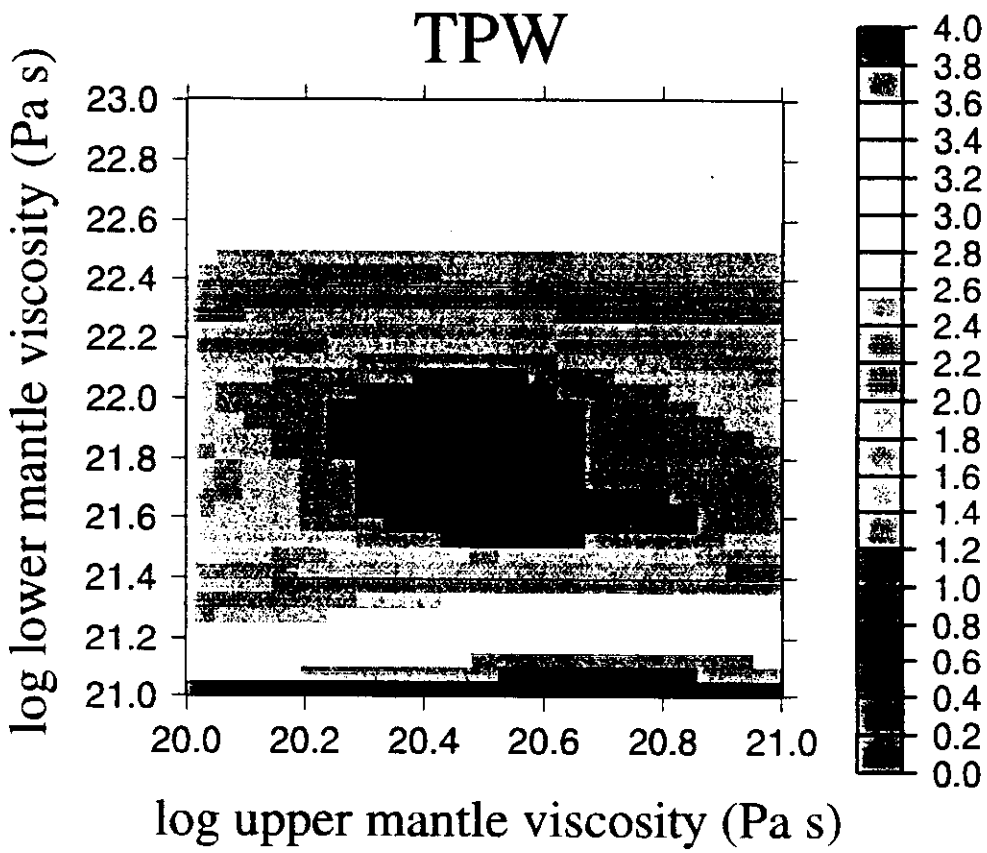

Data (Mc Carthy and Luzum, 1996)

Late Pleistocene deglaciation

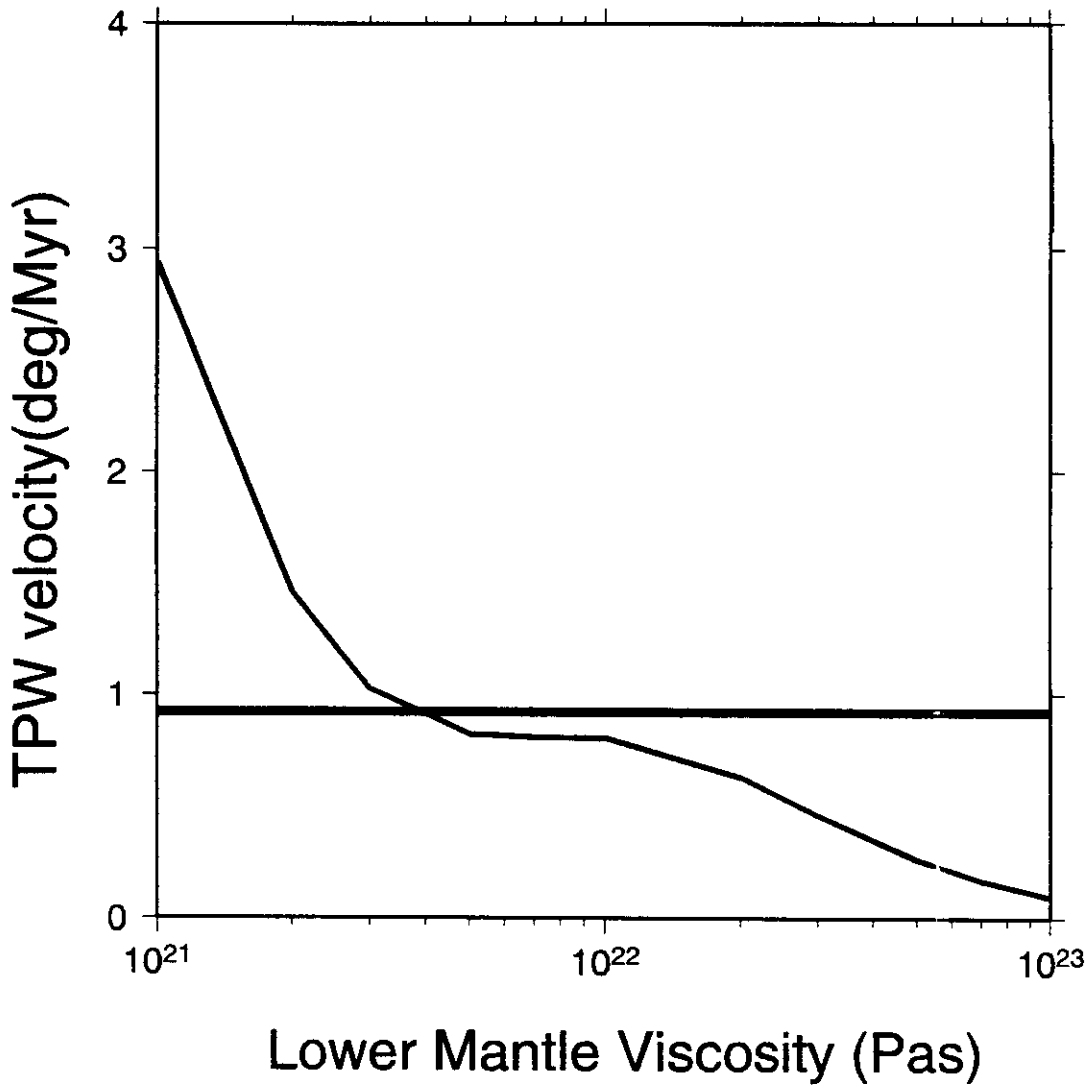

Data (Mc Carthy and Luzum 1996)

LOG CHISQUARE

Antarctica: ½ max negative mass balance

Greenland: mass balance = 0

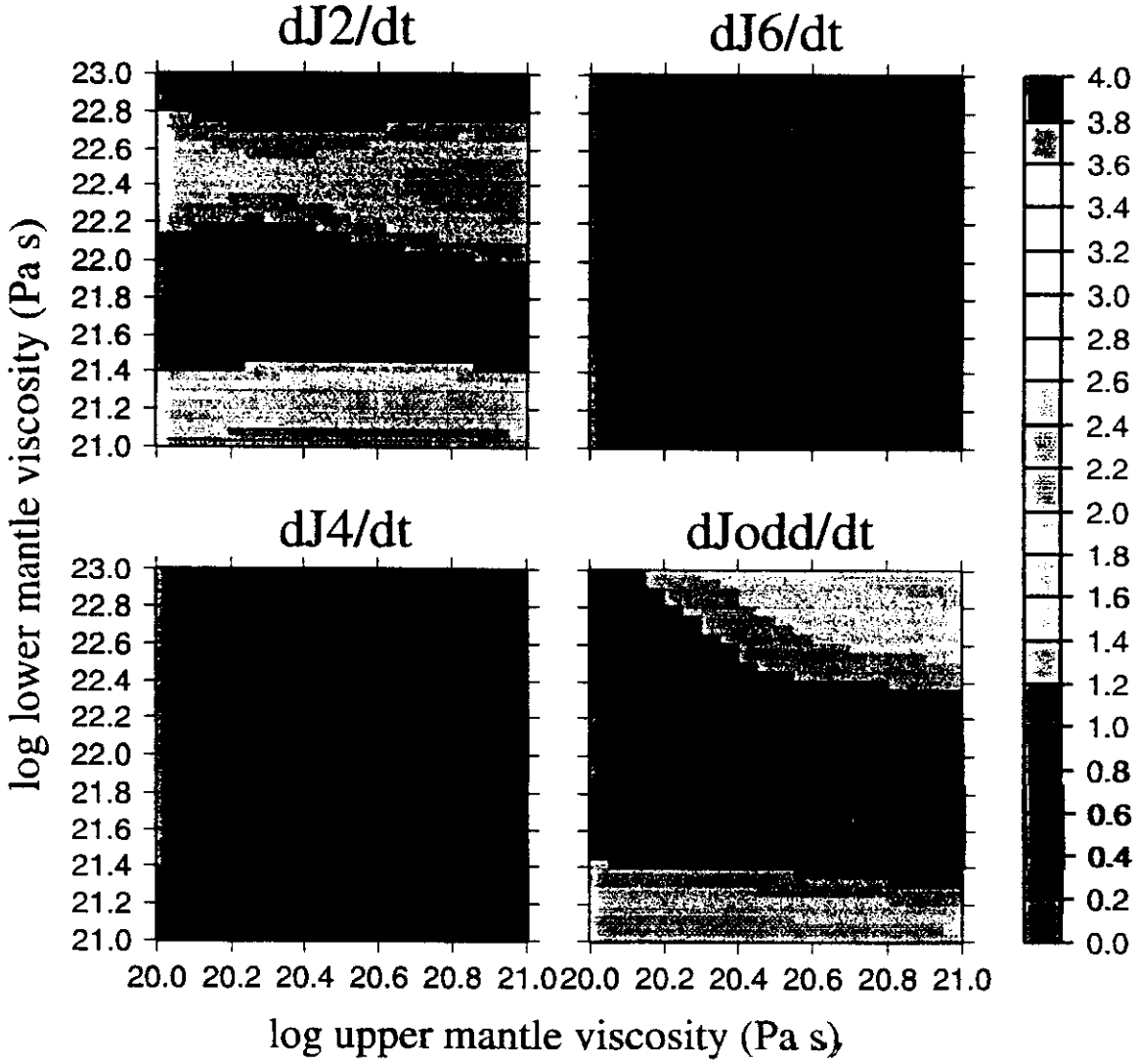

Data (Cheng et al. 1997)

LOG CHISQUARE

Antarctica: ½ max negative mass balance

Greenland: max negative mass balance

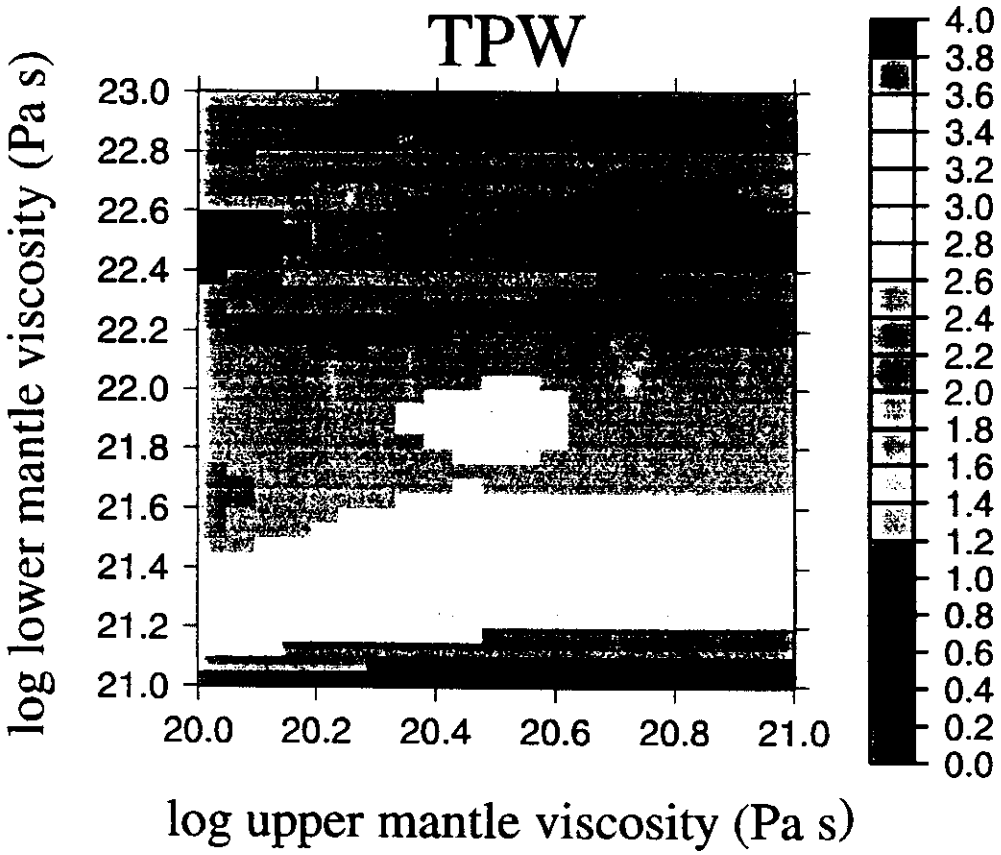

Data (Mc Carthy and Luzum, 1996)

LOG CHISQUARE

Antarctica: ½ max negative mass balance

Greenland: max negative mass balance

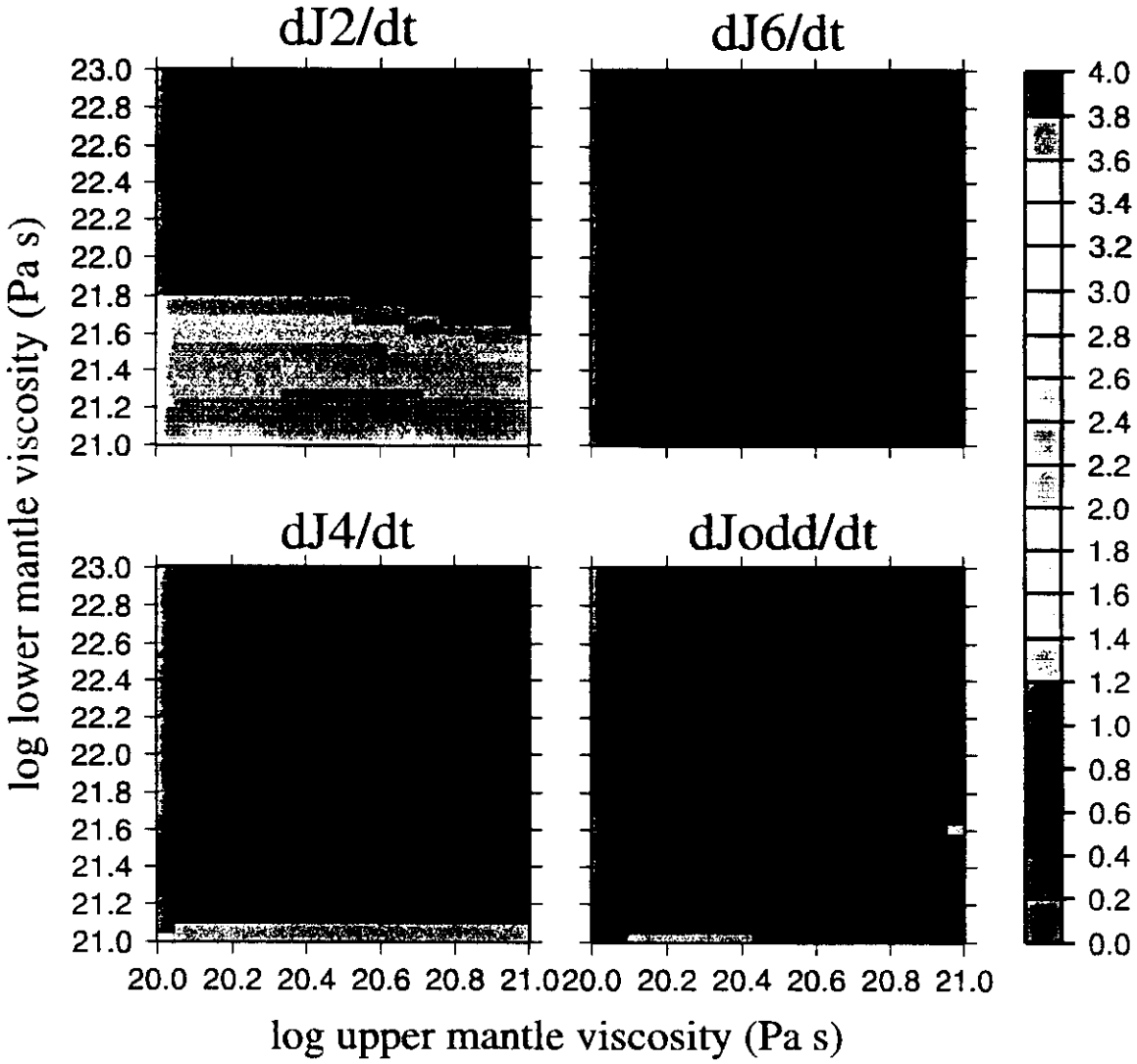

Data (Cheng et al. 1997)

Conclusions

One step ahead with respect to our present-day knowledge of the dynamics of the Earth will be gained in the following decades at the interface between geophysics and geodesy.

We can predict the time evolution of our planet, on time scales that could also interfere with the life-time of human beings.

Geophys. J. Int. (1997) 129, 330–346

Modern tectonic regime in the Tyrrhenian area: observations and models

Gianna Bassi,[1,*] Roberto Sabadini[2] and Samira Rebaï[3]

[1] *Faculty of Earth Sciences, Vrije Universiteit, Amsterdam, the Netherlands*
[2] *Dipartimento di Scienze della Terra, Settore di Geofisica, Università di Milano, Italy*
[3] *Laboratoire de Géophysique et Tectonique, Université de Montpellier II, France*

Accepted 1996 December 20. Received 1996 November 11; in original form 1995 December 21

SUMMARY

The rapid opening, since 10 Ma, of the Tyrrhenian Sea in a context of convergence between Eurasia and Africa remains a puzzling geodynamic problem. One of the most plausible scenarios, proposed by Malinverno & Ryan (1986) attributes extension to southward and eastward migration of the trench, resulting from subduction of the African–Adriatic lithosphere below the European lithosphere. At present, subduction only continues along the Calabrian arc. A compilation of recent strain and stress indicators by Rebaï, Philip & Taboada (1992) indicates that an extensional regime still prevails in the Tyrrhenian Sea, whereas compression dominates north and south of this area. In an earlier paper, Bassi & Sabadini (1994) used a numerical model to demonstrate the necessity of a 'trench suction force', acting along the subduction trench, to produce the present extension in the Tyrrhenian domain. This study, however, did not discuss in detail the tectonic regime in the different areas composing the domain, nor the match between the observations and the model. In this paper, we first review the constraints provided by the observations compiled by Rebaï *et al.* (1992) and by more recent measurements. We then investigate how much of the observed tectonic regime can be understood in terms of plate-interaction forces, using 'thin-plate' models (Bird 1989). The geometry and heterogeneous lithospheric properties of the models are constrained by observations. The best-constrained boundary conditions are held constant; the remaining are regarded as parameters that we tune in order to fit the observations.

Our results indicate that the present-day tectonic regime in the Tyrrhenian area can be explained as a consequence of trench retreat associated with the subduction of Ionian oceanic lithosphere under the Calabrian Arc, combined with a rotation of the Apennines, possibly related to a rotation of the Adriatic microplate. This study supports, therefore, the model of Malinverno & Ryan (1986) and suggests, moreover, that rotation of the Apennines is an ongoing process, which is supported by seismological and geodetic data but remains to be understood in terms of geodynamics. A discrepancy between observations and models is observed in western Sicily, which can be attributed to modelling limitations. The weak extensional activity of the Corsica–Sardinia block, however, is not explained by this model.

Key words: backarc, extension, lithospheric deformation, model, stress distribution, Tyrrhenian domain.

INTRODUCTION

The Tyrrhenian Sea and Apenninic chain (Fig. 1) have attracted considerable attention over the years, producing an abundant literature on the geological and geophysical characteristics of this complex region. Besides the interest in evaluating seismic risk, there is a fundamental interest in understanding the formation of these structures, which developed in the general framework of the Africa/Eurasia collision. In this context of convergence, the rapid opening since Tortonian times of the Tyrrhenian basin represents an intriguing problem. Extension, initially in a W–E and evolving into a NW–SE direction (Patacca, Sartori & Scandone 1990), took place within the

* Now at: Research School of Earth Sciences, Australian National University, Canberra, Australia. E-mail: gianna@rses.anu.edu.au.

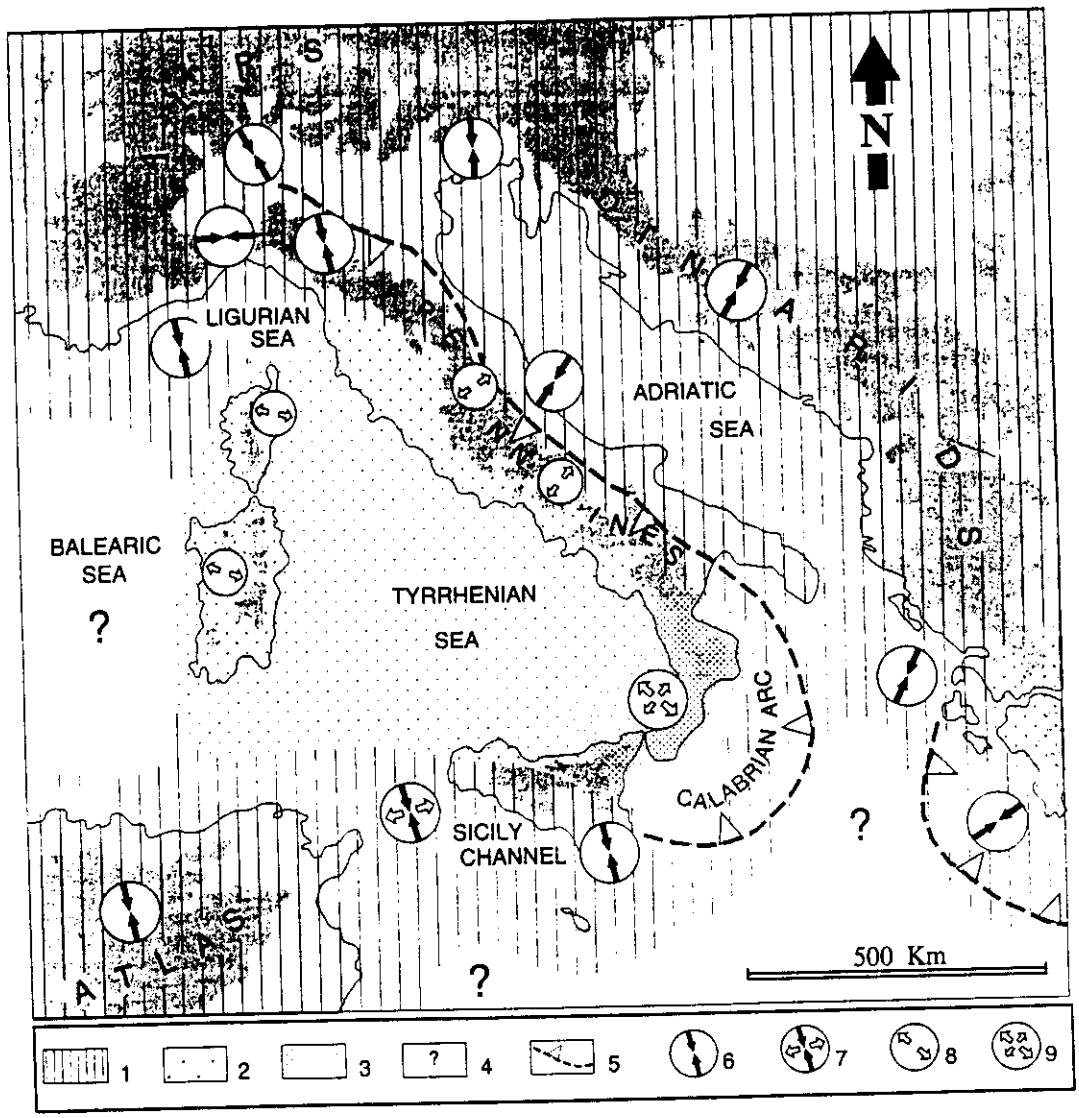

Figure 3. Summary of observations and schematic map of the tectonic zones in the Tyrrhenian area. 1: zone displaying reverse and strike-slip faulting; 2: zone displaying normal and strike-slip faulting; 3: tectonic regime close to radial extension; 4: non-defined regime; 5: thrust front; 6: maximum horizontal compression direction (compressional tectonic context); 7: strike-slip tectonic context; 8: least horizontal stress direction (extensional tectonic context); 9: radial extension.

different areas comprising the domain, nor how well these observations were matched by the model. A first-order comparison of model results and observations shows that extension is predicted in a more restricted area than is actually observed. The cause of this discrepancy lies both in the simplicity of the model itself and in the interpretation and interpolation of data, which show large variations of tectonic stresses, especially in the southeastern Tyrrhenian Sea (Fig. 2). In this paper we discuss in more detail the constraints provided by the observations compiled by Rebaï *et al.* (1992) and by more recent measurements. In a context like this one, where the interpretation of data is controversial, numerical modelling of lithospheric deformation provides additional understanding by indicating what type of boundary conditions can reproduce specific observations, in this case the stress/strain regime. We discuss, therefore, a series of models using the thin sheet approach developed by Bird (1989) and used by Bassi & Sabadini (1994). The geometry and heterogeneous lithospheric properties are chosen according to observations. The best-constrained boundary conditions are fixed; the remaining ones are regarded as parameters that we try to tune in order to obtain a reasonable fit with observations. It is important to emphasize that the focus of this study is the regional tectonic regime in the Tyrrhenian Sea and adjoining areas. As a result, local situations and processes occurring on the boundaries of this domain may be either overlooked or oversimplified. This is the case, for example, of the Apennines, which would require a model of their own. Finally, we discuss the implications of these boundary conditions for the mechanisms currently active in and around the Tyrrhenian area.

MODERN TECTONIC REGIME

The current tectonic regime in the Tyrrhenian area is characterized by a great variability. The causes of this variability probably lie both in the diversity of tectonic forces acting

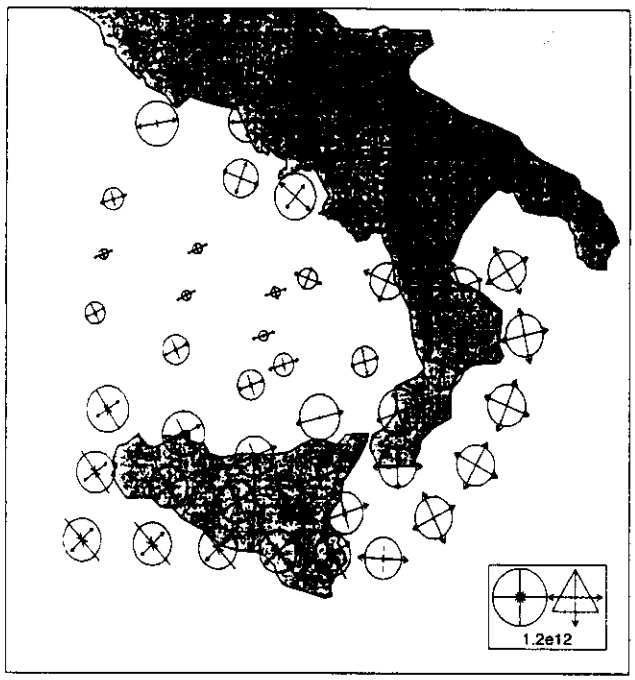

Figure 11. Principal stresses within the Calabrian Arc predicted by Model 3. Note that these are integrated (over the layer thickness) deviatoric stresses, measured by reference to a mid-ocean ridge, i.e. a column of mantle at asthenosphere density, with a 2.7 km deep ocean on top and a 5 km crust. Arrows represent the horizontal stress components, while the vertical stress is represented by a circle (compressional) or a triangle (extensional). Note the almost isotropic state of stress in Calabria.

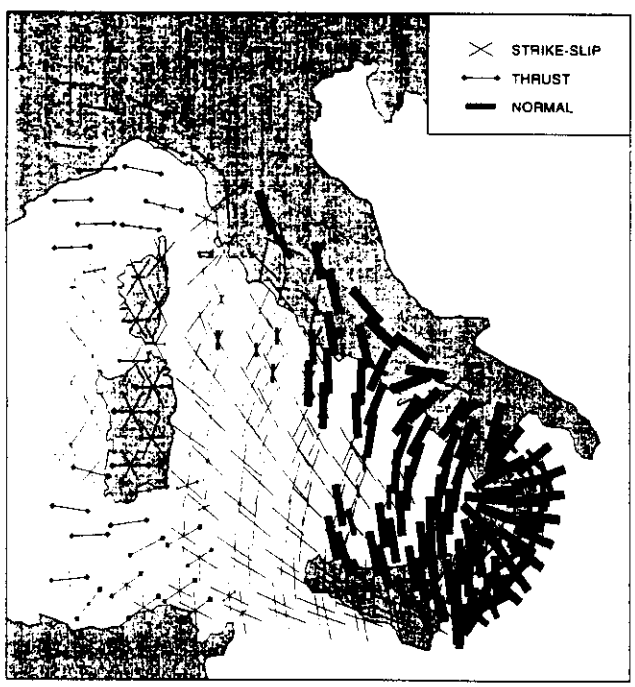

Figure 12. Same as Fig. 10(b), but for a reduced rotation velocity along the Apennines (7.5 mm yr^{-1} instead of 15 mm yr^{-1}). Extension is less widespread in the Tyrrhenian Sea, and the faulting mode in Sardinia becomes dominantly compressional.

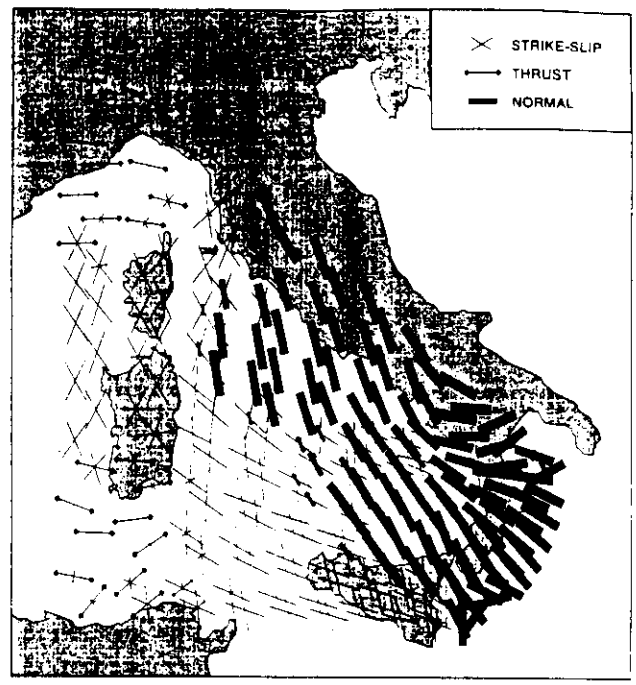

Figure 13. Same as Fig. 10(b), but for a reduced trench suction force (2×10^{12} N m^{-1} instead of 4×10^{12} N m^{-1} over the entire lithosphere). Extension in Calabria becomes dominated by the Apennines rotation and is parallel to the geological structures.

component, imposed by the Apennines rotation, becomes dominant in the extensional pattern of the southeastern Tyrrhenian Sea and Calabria, while the results in the northern half of the domain are the same as in Model 3.

Besides the choice of boundary conditions, the variation of initial lithospheric properties—crustal and mantle thickness, heat flow—across the domain may also contribute to the predicted tectonic pattern by controlling the average rheology at each point and also by determining the level of gravitational stresses that arise due to differences in the density distribution with depth (Artyushkov 1973; Fleitout & Froidevaux 1982). The influence of lateral heterogeneity was tested by running a model with uniform lithospheric properties, specifically a 25 km thick crust and 90 mW m^{-2} heat flow. The faulting mode for such a homogeneous lithosphere (Fig. 14) is smoother but not significantly different than for a heterogeneous lithosphere, which indicates that the results are primarily determined by the boundary conditions. A difference to be noted is the purely strike-slip regime predicted in the Corsica–Sardinia block, compared with the mixed strike-slip/compressional regime observed in Model 3. In turn, the importance of gravitational stresses can be examined by running a model similar to Model 3 but with uniform density (Fig. 15). Again, the only noticeable difference concerns the Corsica–Sardinia block, where the regime is slightly more compressional in the absence of gravitational forces. This means that this continental block does indeed have a tendency to 'spread' under gravitational forces, but the contrast in crustal thickness between the block and the surrounding area is not sufficient to generate significant extensional stresses. This is indeed what is expected for continental crust that is only 30 km thick (Braun & Beaumont 1989).

Geophys. J. Int. (1999) 136, 261–274

Three-dimensional modelling of crustal motions caused by subduction and continental convergence in the central Mediterranean

Ana Maria Negredo,[1,*] Roberto Sabadini,[1] Giuseppe Bianco[2] and Manel Fernandez[3]

[1] *Dipartimento di Scienze della Terra, Università di Milano, Via L. Cicognara, 7, 20129 Milano, Italy. E-mail: annaa sabadini.geofisica.unimi.it*
[2] *Centro di Geodesia Spaziale, Agenzia Spaziale Italiana, Località Terlecchia, C.P. Aperta, 75100 Matera, Italy*
[3] *Institute of Earth Sciences 'J. Almera'—CSIC, Lluis Solé i Sabaris s/n 08028, Barcelona, Spain*

Accepted 1998 August 25. Received 1998 August 25; in original form 1997 November 12

SUMMARY

Crustal deformation in the central Mediterranean is modelled by means of 3-D finite element models assuming a viscoelastic rheology. The tectonic mechanisms under investigation are subduction of the Ionian oceanic lithosphere beneath the Calabrian arc and continental convergence between the African and Eurasian blocks. Very Long Baseline Interferometry (VLBI) data at the station Noto in Sicily and the results from global models of plate motions are taken as representative of the motion of the African plate with respect to Eurasia, while VLBI solutions at Matera and Medicina, in the southern and northern parts of the Italian peninsula, are geodetic observations that must be compared with modelling results. Vertical deformation rates are taken from geological and tide gauge records. The model that best fits the observations includes the effects of subduction in the southern Tyrrhenian and convergence between Africa and Europe.

The overthrusting of the Tyrrhenian domain onto the Adriatic domain results in an eastward component of the velocity at the eastern border of the Tyrrhenian domain, in agreement with VLBI data from the Matera and Medicina stations and GPS data from northeastern Sicily and the Eolian Islands. The highest subsidence rates are obtained in the southern Tyrrhenian, and are of the order of 1.2–1.4 mm yr^{-1}. Along the whole Adriatic coast of the Italian peninsula, subsidence in the foredeeps is of the order of 0.2–0.5 mm yr^{-1}. The Apenninic chain is rising with rates of the order of 0.2–0.4 mm yr^{-1}. Subduction beneath the Calabrian arc is responsible for a roll-back velocity higher than in the northern areas. 2-D models, built for the geological past, indicate the possibility of roll-back velocities of several centimetres per year. In particular, active rifting in the Tyrrhenian and softening of the crust in the back-arc basin result in a trench retreat velocity in agreement with geological estimates. Our results show that numerical modelling can be used to estimate present-day deformation rates and the contribution of active tectonics to sea-level changes along coastal areas.

Key words: 3-D modelling, central Mediterranean, convergence, deformation rate, subduction.

INTRODUCTION

The Mediterranean region is attracting considerable attention due to the complexities of its tectonic setting, which is considered a unique natural laboratory for studying the occurrence of extensional tectonics in a framework of continental convergence.

In this paper, we will focus on the central Mediterranean, the Tyrrhenian basin and surrounding mountain belts; this region is affected by the collision between the African and Eurasian blocks and by the subduction of the Ionian lithosphere. Extension started in the Tortonian within a N–S-trending Alpine orogenic belt west of the Sardinia–Corsica block, and evolved in a different way in the northern and southern parts of the Tyrrhenian basin, with moderate extension in the north and stronger extension in the south, where lithospheric thinning produced oceanic crust (Kastens *et al.* 1987). Extension initiated in the western part of the Tyrrhenian basin

* Now at: Departamento de Geofísica, Facultad de Ciencias Fisicas, Universidad Complutense de Madrid, Ciudad Universitaria s/n, 28040 Madrid, Spain.

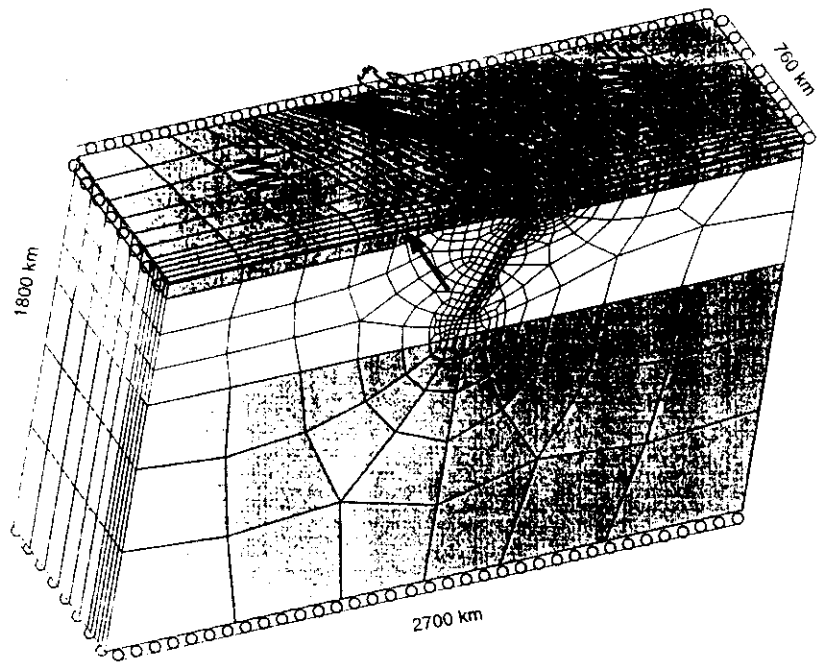

Figure 2. Model geometry, boundary conditions and 3-D finite element mesh used in the calculations. The circles denote a free-slip condition. The arrow denotes the velocity applied in some calculations to the southern boundary of the Tyrrhenian domain to simulate the motion of the African plate. The springs represent the buoyant restoring force applied at the surface.

thick. Due to the high heat flow values measured in the southern Tyrrhenian (Mongelli *et al.* 1991), we have considered a lithospheric thickness of 40 km, whereas a lithospheric thickness of 80 km has been assumed for the northern areas. For the sake of simplicity, the other parameters of the model do not change from south to north and the whole Tyrrhenian domain is assumed to be a continental plate. We have used a linear viscoelastic rheology, with viscosities of 10^{24} Pa s for the crust and harzburgite layer, 5×10^{22} Pa s for the lower lithosphere, 10^{21} Pa s for the asthenosphere and transition layer, and 3×10^{22} Pa s for the lower mantle (Whittaker *et al.* 1992; Spada *et al.* 1992). The elastic parameters are calculated using the PREM reference model (Dziewonski & Anderson 1981). The dip of the slab is 70° and reaches a depth of 500 km. Although some authors suggest that the slab may be totally or partially detached (e.g. Spakman 1990), we have modelled a continuous slab on the basis of the absence of seismicity gaps (Anderson & Jackson 1987; Selvaggi & Chiarabba 1995) and on the results of numerical models (Giunchi *et al.* 1996), which show that the stress pattern and present-day surface motions are better reproduced when assuming a continuous slab. The density anomalies within the slab, due to the phase transformation of a subducting oceanic plate, are based on the petrological model of Irifune & Ringwood (1987) and reach a maximum value of 400 kg m^{-3} at 400 km.

Further to the north, the interaction between the Tyrrhenian and the Adriatic domains is a matter of debate. The presence of subcrustal seismicity down to 90 km (Selvaggi & Amato 1992) together with petrological and geochemical studies (Serri *et al.* 1993) indicate a process of subduction/delamination of the Adriatic lithosphere. However, the existence of a high-velocity body beneath the northern Apennines, representing a detached (Spakman 1990) or continuous slab (Amato *et al.* 1993), is still a matter of debate. Mele *et al.* (1997) showed that a region of shear-wave attenuation exists in the uppermost mantle beneath the northern Apennines. Due to these still controversial results, we have followed the cautious point of view by modelling the dynamics of the Apennines for the Quaternary as a zone of collision between the Tyrrhenian and Adriatic domains. Comparison with geological observations justifies *a posteriori* our hypothesis, and shows that it is not necessary to invoke a process of subduction to explain subsidence and uplift rates in the Adriatic foredeep and northern Apennines, respectively. The underthrusting of the Adriatic lithosphere is assumed to occur via a megathrust (solid triangles in Fig. 3) dipping about 30° and reaching a depth of 90 km.

The density contrasts in the slab and the convergence velocity are activated at time $t=0$ and maintained constant thereafter, following the same procedure as Whittaker *et al.* (1992). After a time interval of about 250 kyr since loading, dynamic equilibrium between the buoyant restoring force and the forces arising from density contrasts and convergence is attained. By this time, the unrealistic initial stress and velocity distribution associated with instantaneous loading have vanished and reached steady-state values: the vertical and horizontal components of the velocity are then sampled at the surface. The timescale of validity of the modelling results is 10^5–10^6 yr, during which the geometric configuration does not change significantly; for longer integration times, viscoelastic models overemphasize the stiffness of the lithosphere.

The velocity vectors shown in Fig. 3 correspond to the CGS-VLBI-EUR96 solution, obtained by the Centre of Space Geodesy of the Italian Space Agency in Matera. Table 1 gives the velocities in mm yr^{-1} of the CGS-VLBI-EUR96 solution for the VLBI stations Noto, Matera and Medicina in the local topocentric reference frame (Lanotte *et al.* 1996). In order to obtain the horizontal components of the velocity with

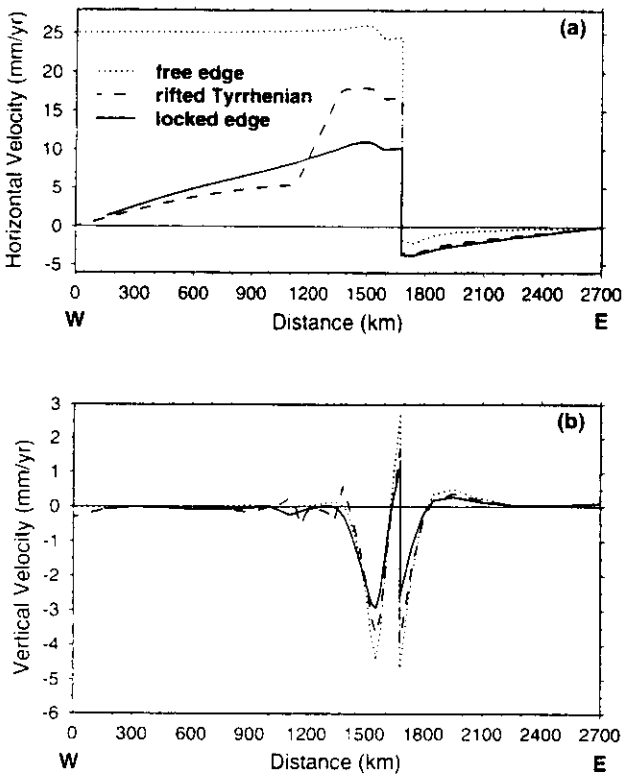

Figure 12. (a) Horizontal and (b) vertical components of the surface velocity obtained with three different 2-D models. The *free edge* model assumes free E–W motion of the left edge. The *rifted Tyrrhenian* model assumes a reduction of the lithosphere viscosity in the area of the basin to account for continental break-up.

geometry and conditions for the geological past, we test some simplified 2-D models with the same geometry and element type as Giunchi *et al.* (1996) in order to study the possible causes of higher roll-back velocities in the past. The horizontal and vertical surface velocities are shown in Fig. 12. Positive and negative values of horizontal velocity denote eastward and westward motions, respectively. The discontinuity at 1675 km corresponds to the location of the hinge line. The model assuming free motion of the left edge of the overriding plate could be representative of an old tectonic setting, when large southward and eastward motions in the Mediterranean allowed the formation of the Balearic and Liguro–Provencal basins and counterclockwise rotation of the Corsica–Sardinia block (Auzende *et al.* 1973). With respect to the fixed edge model (solid line) roll-back is increased by a factor two to nearly 3 cm yr^{-1}. This value is comparable to the high velocities of trench retreat for open oceanic environments, such as in the Pacific.

These results indicate that in a *closed* environment such as the Mediterranean, roll-back velocities of the Calabrian Arc are necessarily lower than those found in oceanic environments such as the Pacific, because of the finiteness of the domain that, at least for the present-day tectonic setting, inhibits the possibility of large displacements of the overriding plate and flow in the mantle.

The free left edge boundary condition is not realistic after the Middle Miocene (about 15 Myr ago), when the Corsica–Sardinia block stopped its counterclockwise rotation (Vigliotti & Langenheim 1995): this event was followed by rifting in the Tyrrhenian. During this phase, hot upper-mantle material replaced the broken continental crust. In our purely mechanical model, this event is modelled by means of decreasing the viscosity of the lithosphere to asthenospheric values, as in the rifted Tyrrhenian model (dashed curve). This reduction causes an increase in the roll-back velocity of about 50 per cent with respect to the reference model (solid line), providing a value that, although underestimating the geologically inferred roll-back velocities quoted above, agrees well with the average velocity of hinge retreat during the last 20 Myr of 2 cm yr^{-1} estimated by Malinverno & Ryan (1986).

Inspection of the lower panel of Fig. 12 indicates that the pattern of vertical motion rates is less affected by the modification in the boundary conditions than the horizontal motions. We notice, however, that the fastest model (dotted line) predicts vertical velocities in the arc and in the trench two times higher than those of the reference model (solid line).

CONCLUDING REMARKS

The generally satisfactory agreement between 3-D modelling results and the crustal motion pattern inferred from geological and geodetic observations indicates that, to first order, the principal tectonic structures and forces have been correctly reproduced, at least for the Plio-Quaternary. Discrepancies between model results and observations in the Tyrrhenian Sea can be attributed to model limitations, since the model does not account for subsidence caused by rifting. The present-day horizontal motion pattern, together with the subsidence in the back-arc basin and in the foredeeps and the uplift of the Apennines can only be reproduced when both subduction in the Calabrian Arc and convergence between Africa and Europe are included in the models. The model that best fits the observations, model 4, assumes that the interaction between the Tyrrhenian and Adria–Ionian domains occurs via an unlocked fault, and that the southern boundary is free to move in the E–W direction.

Although slab-pull alone causes a very low hinge retreat velocity, sinking of the slab strongly enhances the eastward extrusion of the Calabrian arc when convergence is active. This study confirms that subduction beneath the Calabrian arc is responsible for a faster hinge retreat velocity in the southern areas of the model, in agreement with previous studies (Malinverno & Ryan 1986; Faccenna *et al.* 1996; Negredo *et al.* 1997).

Calculated roll-back velocities along the hinge line are clearly smaller than those inferred from geological studies. 2-D models built for the geological past indicate that the roll-back velocity could have been significantly higher in the past, either due to a reduced viscosity in the back-arc basin accounting for active rifting in the Tyrrhenian Sea or due to E–W motion at the western boundary.

ACKNOWLEDGMENTS

This work is financially supported by the EU grant 'Geodynamic modelling of the Western Mediterranean' no. CHRX-CT94-0607 and by the contract no. ARS -96-120 of

resembles that of the model without convergence, owing to the reduced effectiveness of convergence in the locked model. The subsidence maximum results from contributions from the negative buoyancy of the subducted slab and from the flexural response to the exaggerated uplift induced at the southern edge. We have thus noticed that in general all the models have the tendency to overestimate the flexural response of the plates. This is clearly the unavoidable consequence of using continuous plates, while in the real situation deformation is accommodated by faults and aseismic creep. In the central and northern sectors of the peninsula, the uplift disappears, because the Tyrrhenian domain cannot overthrust onto the Adriatic plate, and, for the same reason, subsidence in the Adriatic foredeeps is drastically reduced. It is clear that this locked model fails completely to reproduce the pattern of vertical motions in the whole peninsula and surrounding basins and foredeeps. This is the indication that, at least on the timescale of 10^5 yr, the two sectors of the peninsula, the Tyrrhenian and Adriatic sectors, are decoupled. This decoupling occurs via earthquakes and aseismic creep, as can be seen in the distribution of the earthquakes along the peninsula, which follows the megafault separating the two plates in our model (Pondrelli *et al.* 1995). We can say that the sequence of earthquakes following the Apenninic chain accommodates the slip on the megafault in our model on a geological timescale.

DISCUSSION OF 3-D MODELLING

The two cases that we have considered, totally unlocked and totally locked, are of course two end-members of the real configuration, in which the boundary between the two plates can be partially locked, with heterogeneities along the whole Italian peninsula, and with phases of locking and unlocking at different times. Of course, there is no possibility at the moment of modelling such a complex tectonic situation, so, to first order, we limit our attention to these two end-members, assuming the same coefficient of friction along the whole boundary separating the two plates. Ongoing GPS campaigns will probably provide better constraints on the interaction between the two plates along the Italian peninsula in the near future.

The pattern of vertical and horizontal motions of the surface is reproduced properly by models 2 and 4 (Figs 5 and 8), which include the effects of subduction under the southern Tyrrhenian Sea and convergence between Africa and Eurasia. Discrepancies between model predictions and observations in the southern Calabrian arc and in the Tyrrhenian Sea are attributed to model limitations.

Fig. 11 shows in detail the variation of roll-back velocity along the modelled subduction hinge line for the set of models using an unlocked fault. This velocity is calculated as the difference at the hinge line between the horizontal E–W velocities of the overriding and subducting plates. The most evident features of this figure are the high variability of roll-back velocity among the different models and the location of the maximum at the southern part of the study area, corresponding to the subduction zone. The latter result demonstrates the major role of slab-pull in controlling the velocity of trench retreat on timescales of 10^5 yr.

Models carrying solely a subducted plate without convergence (models 1 and 3) produce insignificant roll-back

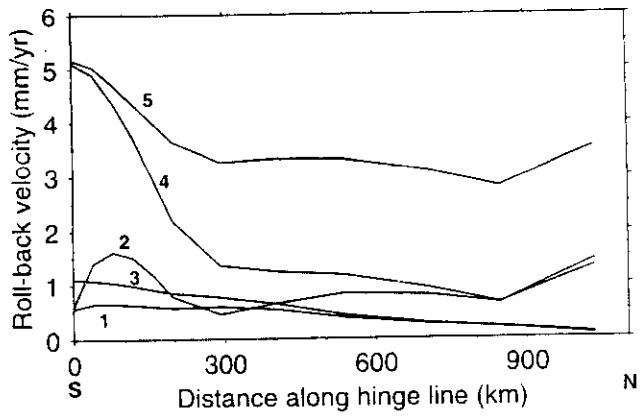

Figure 11. Variation of the roll-back velocity along the modelled hinge line, obtained for the models (indicated by the labels) with an unlocked fault.

values. The effects of subduction on roll-back velocity are enhanced when convergence is activated and E–W motion of the southern boundary is permitted (models 4 and 5): strong variations of roll-back velocity occur along the hinge line. At the subduction zone, roll-back increases from 1 mm yr^{-1} in model 3 to 5 mm yr^{-1} in models 4 and 5, while a substantial reduction is observed along the hinge line. In the northern sectors of the peninsula, the presence of the Adriatic plate counteracts the eastward extrusion of the Apenninic chain, whereas further to the south, the sinking of the slab permits the [illegible] Arc. Our results indicate that slab sinking acting roughly at right angles to continental collision has the effect of 'opening the door' to the escape of crustal material, favouring faster roll-back velocities at the subduction zone.

2-D MODELLING OF THE GEOLOGICAL PAST

Geological estimates based on the migration of hinterland extensional and foreland compressional basins indicate a rate of trench retreat since the Tortonian of 5–6 cm yr^{-1} for the southern Calabrian Arc and 1.5–2 cm yr^{-1} for the northern Apennines (Patacca *et al.* 1990; Cipollari & Cosentino 1994). Model 4 provides an average roll-back velocity in the southern area three times higher than in the northern area, in agreement with the geologically observed trend. However, the precise values are not comparable, because modelling of the tectonic evolution since Tortonian times would require modification of the geometry of the plates and a softer rheology, appropriate for timescales of 10^7–10^8 yr (Gurnis *et al.* 1996). In general, all the models shown in the previous figures predict roll-back velocities lower than those estimated from geological records; possible causes could be the stiffness of the 3-D mesh and the simplified rheology and geometry of the models.

We have seen, on the other hand, that roll-back is extremely sensitive to the geometry and boundary conditions imposed on the model in the vicinity of the subducted slab, and it could well be that modelled velocities derived for the present-day tectonic setting are not representative of the geological past. Since it is impossible to establish with the necessary precision the

Geophys. J. Int. (1999) 139, 98–114

The onset of extension during lithospheric shortening: a two-dimensional thermomechanical model for lithospheric unrooting

Anna Maria Marotta,[1,*] Manel Fernàndez[1] and Roberto Sabadini[2]

[1] *Institute of Earth Sciences 'J.Almera', CSIC, Lluis Solé i Sabaris, s/n 08028 Barcelona, Spain*
[2] *University of Milano, Department of Earth Sciences, Via L. Cicognara 7, 20129 Milano, Italy*

Accepted 1999 May 12. Received 1999 May 6; in original form 1998 July 18

SUMMARY

We model the evolution of the lithosphere during its shortening and consequent gravitational collapse with special emphasis on the induced variations in the surface stress regime and dynamic topography. In particular, we analyse the conditions leading, immediately after lithospheric failure, to local extension, eventually coeval with compression. Different crustal rheologies and kinematic conditions as well as thermally imposed mechanical rupture are considered. Numerical calculations have been performed by using a 2-D finite element code that couples the thermal and mechanical equations for a Newtonian rheology with a temperature-dependent viscosity. The results show that, after the failure of a gravitationally unstable lithospheric root, the replacement of lithospheric mantle by warmer asthenospheric material induces a considerable variation in the dynamic topography and in the surface stress regime. The occurrence of local extension, its intensity and its spatial distribution depend mainly on whether convergence continues throughout the process or ceases after or before the lithospheric failure. Similarly, uplift/subsidence and topographic inversion are controlled by kinematic conditions and crustal rheology. Mechanical rupture produces drastic changes in the surface stress regime and dynamic topography but only for a short time period, after which the system tends to evolve like a continuous model.

Key words: extension, gravitational collapse, lithospheric shortening, topographic instability.

INTRODUCTION

During the last decade, the mechanism of lithospheric mantle removal has attracted the interest of geologists and geophysicists since it can explain the conversion from thrust faulting to normal faulting in continental regions undergoing continuous convergence. A common characteristic of the areas where this mechanism has been invoked is the delay between the initiation of shortening and the onset of extension, which can span several million years, and the huge vertical movements of the Earth's surface associated with this transition (see Houseman & Molnar 1997 for a wide-ranging review of geological settings where mantle removal could operate).

The simplest explanation for the onset of extension under regional compression is the variation in the balance of tectonic forces produced by either an increase in the local potential energy or a change in the convergence velocity. England & Houseman (1988), assuming a thin sheet viscous model, showed that the convergence between plates should cease in order for the gravitationally induced extensional forces to dominate over the compressive ones. However, cessation of convergence cannot account for regions where extension appears to be coeval with regional plate convergence. Furthermore, Fleitout & Froidevaux (1982) and more recently England & Houseman (1989) for a wider range of crustal and lithospheric thicknesses showed that during shortening the potential energy can decrease, rather than increase, due to mantle thickening. Under these conditions, compression is enhanced if no additional mechanisms such as convective removal of the lithospheric mantle lead to an abrupt increase of local potential energy.

This mechanism is based on the idea that lithospheric shortening produces crustal and lithospheric thickening with a consequent downward deflection of the isotherms at deep crustal and lithospheric levels. Under these conditions the lithospheric mantle root, colder and thus denser than the surrounding mantle, becomes gravitationally unstable and sinks into the asthenosphere like a blob. Analysis of the gravitational instability of a thickened lithosphere has been developed by many authors (e.g. Houseman *et al.* 1981; Buck & Toksoz 1983; Houseman & Molnar 1997; Marotta *et al.* 1998; Schott & Schmeling 1998).

* Now at: GFZ, Potsdam 3.4, Telegrafenberg, D14473 Potsdam, Germany. E-mail: marotta@gfz-potsdam.de.

values of kinetic energy at the maxima. Interruption of the convergence reduces these maxima, this reduction being more effective in the case in which convergence has been stopped when the lithospheric thickness has increased by only 30 per cent. Interruption of the convergence has the largest effects for the higher convergence rate of 1 cm yr^{-1} (b). As expected, the high convergence rate has the effect of displacing the maxima in the kinetic energy to the left, indicating that the unrooting process is generally faster for the higher convergence rate. Another remarkable result is that the interruption of convergence has the largest effects in the case of the highest convergence rate; after the interruption of convergence, the values of the maxima for the two convergence rates (a and b) become comparable, indicating that after the termination of convergence the process is mainly controlled by gravitational forces. In Fig. 7 we compare the time evolution of the kinetic energy for two classes of models, without mechanical rupture (thick continuous and dashed curves) and with mechanical rupture (thin continuous and dashed curves), for convergence rates of 0.2 cm yr^{-1} (a) and 1 cm yr^{-1} (b). Both continuous convergence and convergence until lithospheric failure are considered (continuous and dashed curves, respectively). The thick continuous and thick dashed curves in these panels are thus identical to the thick solid and dashed curves shown in Fig. 6 for a continuous convergence and convergence interrupted at lithospheric failure. The most remarkable result of this case study is the increase in kinetic energy for the whole set of models considered when the viscosity along the predefined rupture channel is reduced to simulate the mechanical rupture. The detached lithospheric blob falls almost freely into the mantle, thus increasing the kinetic energy of the system. The largest increase in the kinetic energy, of about the 50 per cent, occurs for the slow convergence rate of 0.2 cm yr^{-1} (a). In the case of fast and continuous convergence (b) the increase is limited to at most 20 per cent; for fast convergence until lithospheric failure, the increase in the kinetic energy is slightly higher, of the order of 30 per cent, as indicated by the curves at the bottom of (b). These results indicate the major effects of mechanical rupture on the kinetic energy of the system when gravitational forces become dominant with respect to horizontal forces. A noteworthy feature characterizing all the calculations is that the time span necessary to complete the process of unrooting remains essentially constant, in spite of the increase in the kinetic energy when the mechanical rupture is introduced. Thermal re-equilibrium occurs a few million years after mechanical rupture, independent of the convergence velocity, implying that deep deformation at long times follows the same pattern as the continuous (non-ruptured) model.

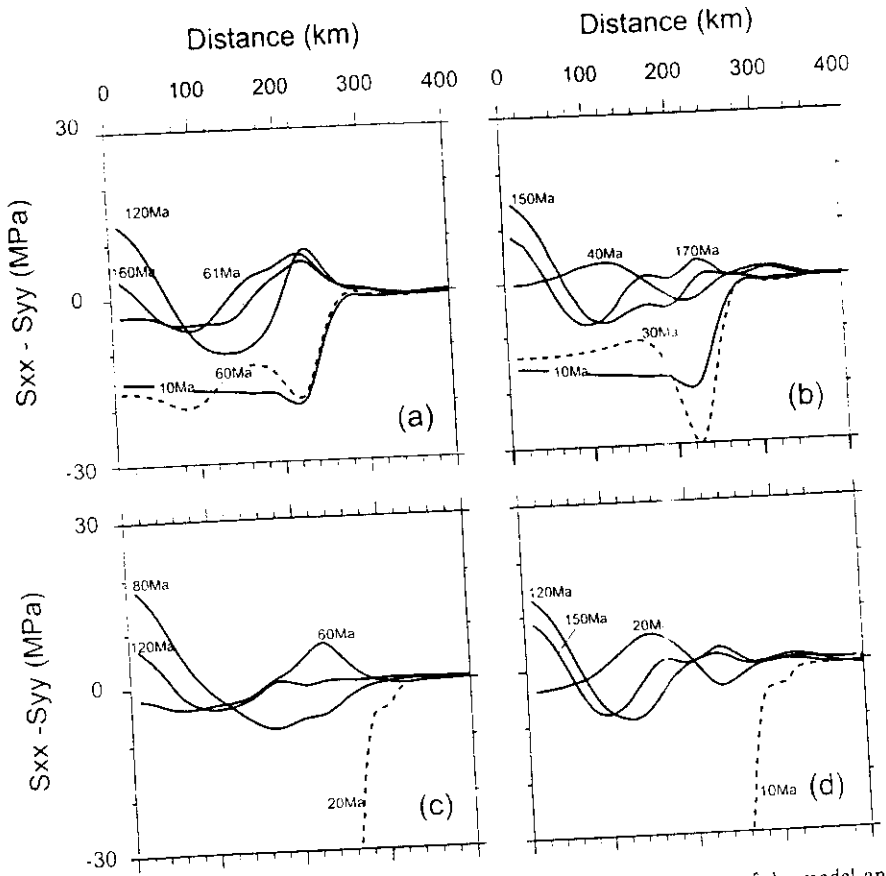

Figure 9. Surface differential stress (positive values indicate extension) versus distance from the centre of the model and for different times in the case when convergence ceases during the orogenic growth stage, before lithospheric failure. Initial convergence with $U_c = 0.2$ cm yr^{-1} that ceased at (a) 60 Myr (corresponding to a change in the thickness of the root of 100 per cent) and (b) 30 Myr (corresponding to a change in the thickness of the root of 50 per cent), and initial convergence with $U_c = 1.0$ cm yr^{-1} that ceased at (c) 20 Myr (corresponding to a change in the thickness of the root of 100 per cent) and (d) 10 Myr (corresponding to a change in the thickness of the root of 50 per cent) are considered for the constant-viscosity crust model. Dashed lines refer to the times when the condition of forced convergence is eliminated and replaced with a condition of no shear stress.

Lenardic & Kaula (1995) made a quantitative evaluation of the surface stress but their analysis was limited to the average value in the centre of the thickened region, and the effects produced by a change in kinematic conditions were not considered. Houseman & Molnar (1997), using a Rayleigh–Taylor instability model, showed that rheology has a strong influence on determining the conditions for mantle convective thinning and that non-linear rheologies can explain the delay between extension and compression. These authors assumed that extension is a consequence of the removal of the lithospheric mantle and no stress calculations were performed. Marotta *et al.* (1998) used a thermomechanical approach with a Newtonian rheology and a temperature-dependent viscosity for the whole system (crust, lithospheric mantle and sublithospheric mantle) to analyse the evolution of the lithosphere–asthenosphere system when subjected to tectonic convergence. The analysis of variations in maximum shear stress, strain rate and total kinetic energy allowed them to define four different stages that characterize the mantle unrooting process (Fig. 1):

(1) a stage of orogenic growth due to tectonic convergence until a critical lithospheric root thickness, about a factor of two of the initial value, is reached;

(2) initiation of gravitational instability of the lithospheric mantle root until the critical conditions for its break-up are reached, when the local shear stress and strain rates have attained a maximum; in the following we will refer to this critical condition as lithospheric failure;

(3) detachment of the lithospheric root and sinking of the root into the sublithospheric mantle;

(4) relaxation of the system towards a new state of equilibrium.

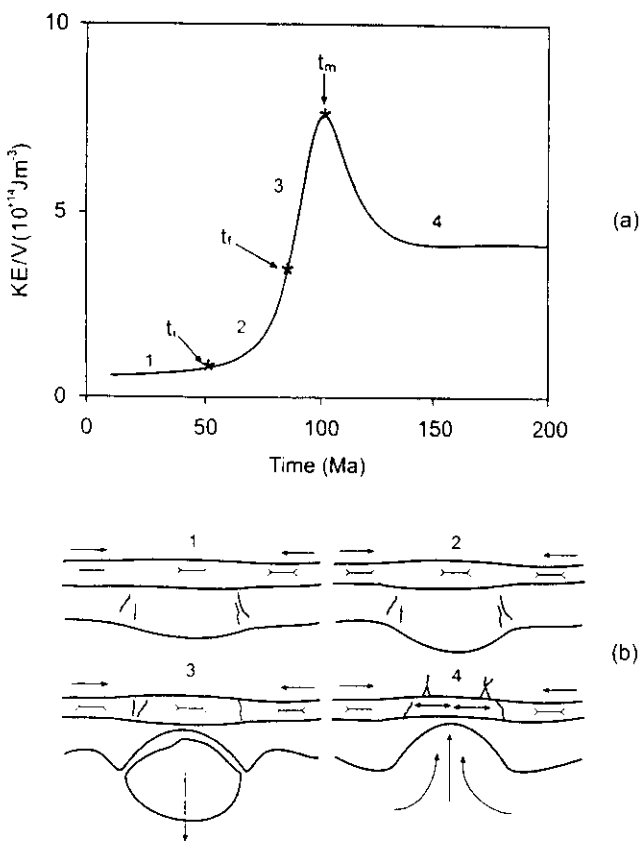

Figure 1. (a) Major stages of the evolution of mantle unrooting deduced from the variation of total kinetic energy. (b) Schematic representation of the unrooting process: (1) orogenic growth, (2) initiation of gravitational instability until lithospheric failure, (3) sinking of the detached lithosphere, and (4) relaxation of the system. Reprinted from Marotta *et al.* (1998), with permission from Elsevier Science.

Although these authors examined the possibility of tectonic inversion after lithospheric unrooting, the use of a single rheology for the whole system prevented them from drawing firm conclusions about the evolution of the surface stress regime. This work was a continuation of that of Marotta *et al.* (1998) and built upon the approach and results of the earlier work.

The main goal of this paper is to analyse the prevailing surface tectonic regime and vertical movements associated with the detachment and subsequent sinking of the lithospheric mantle root after its plastic failure (Ranalli 1987) as a consequence of tectonic convergence. We evaluate the effects of considering different crustal rheologies (constant crustal viscosity and a low-viscosity channel in the lower crust), and different kinematic conditions (continuous convergence versus cessation of convergence at different deformation stages). Different thermal conditions are imposed on the model to simulate mechanical rupture in the lithospheric mantle. The numerical approach has been developed in two dimensions and therefore we will address the primary features associated with lithospheric collapse rather than apply our modelling to specific geological settings.

NUMERICAL MODEL

The physics, parameters and initial and boundary conditions of the numerical model are very similar to those used by Marotta *et al.* (1998), and therefore in this section we will remark only on the main aspects of the model. The reader is referred to the paper mentioned above for a more detailed description. We assume that the system, formed by the lithosphere and the sublithospheric mantle down to 700 km depth, can be approached as a Newtonian fluid. Although our approach does not permit simulation of all the deformation processes, in particular those related to brittle failure, it does allow us to analyse the gross mechanical behaviour during lithospheric convergence, since the Newtonian rheology reproduces the continuum average properties of a discontinuous medium well. Furthermore, the use of a simple linear rheology allows us to address the main factors that control deformation until lithospheric failure: a non-linear rheology would have the effect of localizing and accelerating the strain (Houseman & Molnar 1997).

The dynamics of a Newtonian fluid are governed by the equations of conservation of mass, momentum and energy, which can be expressed in the form

$$\nabla \cdot \mathbf{v} = 0, \tag{1}$$

$$0 = \nabla \cdot (2\mu\dot{\boldsymbol{\varepsilon}}) + \rho\mathbf{g} - \nabla p, \tag{2}$$

$$\rho c\left(\frac{\partial T}{\partial t} + \mathbf{v} \cdot \nabla T\right) = \rho c k \nabla^2 T + H_e, \tag{3}$$

where $\dot{\boldsymbol{\varepsilon}}$ is the strain rate tensor, $\mathbf{v}$ is the velocity vector, μ is the viscosity, p is the pressure, T is the temperature, c is the thermal capacity, k is the thermal diffusivity and H_e is the heat